This is the peer-reviewed, final accepted version for American Mineralogist, published by the Mineralogical Society of America.
The published version is subject to change. Cite as Authors (Year) Title. American Mineralogist, in press.
DOI: https://doi.org/10.2138/am-2020-7534. http://www.minsocam.org/

Revision 3

Iron isotope fractionation in reduced hydrothermal gold deposits: A case study from the Wulong gold deposit, Liaodong Peninsula, East China

JIAHAO ZHENG[1*], BIN CHEN[1*], SHUAIJIE LIU[1], CHUANG BAO[1]

[1] *Department of Earth and Space Sciences, Southern University of Science and Technology, Shenzhen 518055, China*

**Corresponding authors at: No. 1088, Xueyuan Road, Nanshan District, Shenzhen, Guangdong, China. E-mail addresses: joey-zen@163.com (J. Zheng), chenb6@ sustech.edu.cn (B. Chen).*

ABSTRACT

Iron isotope fractionation in hydrothermal systems is a useful diagnostic tool for tracing ore-forming processes. Here, we report on the Fe isotopic compositions of a suite of hydrothermal minerals from ores (pyrite, pyrrhotite, and quartz) from the Wulong gold deposit, Liaodong Peninsula, East China. Pyrites from quartz sulfide ores show a δ^{56}Fe (^{56}Fe/^{54}Fe in the sample relative to IRMM-14) variation from +0.11 ± 0.03‰ to +0.78 ± 0.03‰ (2SD), and pyrrhotites from the same vein are isotopically lighter than the pyrite, varying between -0.85 ± 0.01‰ and -0.07 ± 0.00‰. This result is consistent with theoretical predictions of equilibrium fractionation and published mineral compositions. For the first time, to our knowledge, we report the Fe isotopes of hydrothermal quartz that record the isotopic compositions of the ore-

22 forming fluids. Two quartz separates in the quartz-sulfide vein yield δ^{56}Fe values of -0.02 ±
23 0.02‰ and +0.07 ± 0.07‰, respectively. Our Fe isotope fractionation calculations show that
24 pyrrhotite with light Fe isotopes crystallized first from the ore-forming fluids, which indicates a
25 relatively reduced condition for the initial ore-forming fluids. Then the remaining fluids with
26 heavy Fe isotopes precipitated pyrites with positive δ^{56}Fe values, and their mineral crystallization
27 sequence records an increase of oxygen fugacity during mineralization.
28 Gold deposits in Wulong and Jiaodong share many similar geological characteristics. The
29 pyrites from the Wulong deposit have higher δ^{34}S values (+0.5‰ to +4.1‰) than the pyrrhotites
30 (-1.2‰ to +1.2‰). Pyrites from the Jiaodong gold deposits show a wide range of both positive
31 and negative δ^{56}Fe values as well as high δ^{34}S values, whereas those from the Wulong deposit
32 have a relatively narrow range of positive δ^{56}Fe values and near-zero δ^{34}S values. The
33 differences in Fe isotopes may be due to early precipitation of pyrrhotite with light Fe isotopes
34 under a relatively low oxygen fugacity environment in the Wulong deposit, resulting in pyrite
35 precipitated from the remaining fluids with heavy isotopes. The sulfur isotope variations between
36 Wulong and Jiaodong gold deposits reflects differences in their source regions rather than
37 oxygen fugacities. In addition, we have compiled Fe isotopic compositions of pyrite and
38 pyrrhotite from different types of ore deposits to investigate their Fe isotopic behavior in
39 magmatic-hydrothermal systems. Pyrite grains show a wide range of δ^{56}Fe values. Positive pyrite
40 δ^{56}Fe values reflect an equilibrium isotope effect, whereas negative pyrite δ^{56}Fe values may be
41 due to kinetic isotope effects or to a mixture of sedimentary host rocks. Pyrrhotite grains show
42 similar negative δ^{56}Fe values, and they have strong influence on the Fe isotope systematics in
43 magmatic and hydrothermal systems. Our data show that Fe isotopes can be used to trace

precipitation orders of pyrite and pyrrhotite and oxygen fugacity evolution in relatively reduced hydrothermal deposits.

Keywords: Fe isotopes; Reduced hydrothermal gold deposits; Wulong gold deposit; Liaodong Peninsula

1. Introduction

The formation of ore deposits includes transportation and concentration of elements from the source regions. Iron, sulfur, and oxygen are the main components of ore minerals (sulfides and oxides) in various magmatic-hydrothermal deposits, and sulfur and oxygen isotopic components have been widely used to trace the source of metals and evolution of hydrothermal fluids (Goldfarb et al. 1991; Zürcher et al. 2001; Meinert et al. 2003; Chang et al. 2008; Shanks 2014; Zheng et al. 2017, 2020). Iron isotopes are much less well-studied, owing in part to the lack of fractionation factors. Recent studies yielded mineral-fluid Fe isotope fractionation factors (Polyakov and Soultanov 2011; Syverson et al. 2013; Dauphas et al. 2017), which pave the way for more widespread use in understanding mineralization processes in mineral deposits (Knipping et al. 2015; Bilenker et al. 2016; Mathur and Wang 2019).

Recent studies have shown that Fe isotopes can be fractionated in various ore-forming systems, resulting in wide δ^{56}Fe variations. To date, an increasingly diverse array of Fe isotopic compositions of magmatic-hydrothermal systems has been reported, which include modern seafloor hydrothermal vents (Sharma et al. 2001; Rouxel et al. 2008), skarn deposits (Graham et al. 2004; Wang et al. 2011), porphyry Cu-Au deposits (Wawryk and Foden 2017; Li et al. 2018), iron oxide-apatite deposits (Bilenker et al. 2016; Childress et al. 2016; Knipping et al. 2019;

Troll et al., 2019), hydrothermal Sn-W deposits (Wawryk and Foden, 2015), magmatic Ni-Cu deposits (Bilenker et al. 2018; Ding et al. 2019; Zhao et al. 2019), and layered intrusions (Schoenberg et al. 2009; Bilenker et al. 2017). Orogenic gold deposits formed in relatively oxidized environments have also been studied (Zhu et al. 2018). However, Fe isotopes of gold deposits formed under relatively reduced conditions remain poorly understood.

Heavy Fe isotopes are preferentially incorporated into sites with stronger chemical bonds. Since Fe^{3+} forms stronger bonds than Fe^{2+}, ferric compounds tend to have heavier Fe isotopic compositions (Schauble et al. 2001). Because Fe^{3+} and Fe^{2+} have different melt/mineral equilibrium partition coefficients (Dauphas et al. 2009), it has been well established that redox state controls Fe isotope fractionation during high temperature magmatic processes (Sossi et al. 2012; Dauphas et al. 2014; Foden et al. 2015). In magmatic-hydrothermal systems, Fe is mainly present as Fe^{2+}_{aq} (Chou and Eugster 1977; Simon et al. 2004), and significant Fe isotope fractionation is observed between precipitation of Fe^{2+} species and Fe^{3+} bearing minerals (Markl et al. 2006; Johnson et al. 2008; Steinhoefel et al. 2010). In sulfide hydrothermal systems, Fe^{2+} iron sulfides are the predominant ore minerals, and significant Fe isotope fractionation is observed under pyrite-rich hydrothermal conditions (Zhu et al. 2018). Like pyrite, pyrrhotite ($Fe_{1-x}S$) contains almost exclusively ferrous iron (Mikhlin and Tomashevich 2005) but formed under relatively reduced conditions (Cooke et al. 1996). Thus, the precipitation orders of pyrite and pyrrhotite in the hydrothermal systems can be used to evaluate the evolution of the redox state in relatively reduced hydrothermal deposits. The initial redox condition and evolution of gold deposits are important because they can provide valuable information for the source of ore-forming materials and further exploration strategies.

Pyrite and pyrrhotite are common major Fe-bearing minerals in various hydrothermal deposits. Hydrothermal gold deposits with pyrite as the main ore minerals show a wide range of δ^{56}Fe values for pyrite, varying from -0.78‰ and +0.79‰ (Zhu et al. 2018). By contrast, pyrrhotite preferentially incorporates the light Fe isotope in magmatic-hydrothermal systems, and the presence or absence of pyrrhotite strongly affects the Fe isotope compositions of other minerals (Wawryk and Foden 2015, 2017).

Located in the Liaodong Peninsula, East China, the Wulong deposit is a large hydrothermal gold deposit (>80t at 5.35 g/t) with pyrite and pyrrhotite as main ore minerals, indicating a relatively reduced hydrothermal environment. Thus, it provides an ideal opportunity to investigate Fe isotope variations in reduced hydrothermal gold deposits. In this paper, we present Fe-S isotopic compositions from ore minerals (pyrite, pyrrhotite, and quartz) from the Wulong gold deposit with aims to (1) investigate the initial redox state of reduced gold deposit and its evolution during mineralization, and (2) evaluate the control of pyrrhotite on the Fe isotope system. In addition, combined with previously published Fe isotopic data of pyrite and pyrrhotite from different types of other deposits (Johnson et al. 2003; Wang et al. 2011, 2015; Wawryk and Foden 2015; Bilenker et al. 2018; Li et al. 2018; Zhu et al. 2018; Ding et al. 2019), we summarize their distribution patterns and discuss the causes of their mineral Fe isotopic compositions.

2. Geologic Setting

The Liaodong Peninsula is located in the eastern part of the North China Craton (Fig.1a), adjacent to the well-known Jiaodong gold province. It consists of Early Archean to Paleoproterozoic basement rocks overlain by unmetamorphosed thick Meso- Neoproterozoic and

Paleozoic sedimentary sequences, and magmatic activity was weak until the Mesozoic time (Yang et al. 2007). Large volumes of Mesozoic intrusive rocks crop out in the Liaodong Peninsula, mainly granitoids with minor diorites and mafic dikes (Fig.1b). Most of the intrusions were emplaced during the Early Cretaceous (131-117 Ma), and others formed in Jurassic (180-156 Ma) and Late Triassic (233-212 Ma) (Wu et al. 2005). The Late Triassic magmatism occurred in a post-orogenic lithospheric delamination related extensional setting (Yang et al. 2007). The Jurassic magmatism was generated by westward subduction of paleo-Pacific plate, and Early Cretaceous igneous rocks were formed due to a collapse of the thickened continental crust (Wu et al. 2019).

Several gold deposits are present in the Liaodong Peninsula, including the Wulong, Sidaogou, and Xinfang deposits in the eastern part, and the Baiyun, Linjiasandaogou, and Xiaotongjiapuzi deposits in the western part (Fig.1b). The Wulong gold deposit is one of the largest gold deposits in the eastern part of the Liaodong Peninsula. The stratigraphy of the Wulong ore field comprises predominantly Quaternary sediments, and major faults strike NNE and NW (Fig.2a). The Wulong granite is the main ore-hosted rock in mining area (Fig.2), and has a SHRIMP zircon U-Pb age of 163 Ma (Wu et al. 2005). Many NNE-trending diorite, granite porphyry, lamprophyre, and diabase dikes intruded the Wulong granite (Fig.2a and b). The diorite dikes are spatially related to auriferous quartz-sulfide veins, and they have a zircon U-Pb age of 123 Ma (Liu et al. 2019). Some diabase dikes crosscut the quartz-sulfide veins.

To date, a total of 380 auriferous quartz-sulfide veins have been identified in the Wulong deposit with No. 163 vein as the largest orebody (Fig.2a). The thick quartz vein is the main ore source of Wulong gold deposit, accounting for more than 99% of the total ores. The No.163 vein is now mined underground at depths of several hundred meters below sea level (Fig.2b). Only a

few disseminated pyrites were observed in the altered diorite (Fig.4a and e), which was crosscut by quartz-sulfide veins (Fig.4b). Auriferous quartz-sulfide veins are the predominant ores in the Wulong deposit, and they vary from ~1 cm (Fig.4b) to more than 1 m (Fig.3). Ore minerals in the quartz-sulfide orebodies are composed predominantly of pyrite and pyrrhotite, and minor bismuth tellurides, chalcopyrite, and native gold (Fig.4 c, d, and f). Native gold commonly occurs within pyrite, pyrrhotite, and quartz as small composite inclusions (~5μm to ~60 μm), which mainly consist of native gold, bismuthinite, and hedleyite. Pyrite and pyrrhotite are homogeneous in composition, no chemical zonations were reported by previous studies or observed in this study.

Fluid inclusion volatiles from the Wulong deposit are dominated by H_2O-CO_2-CH_4, and temperatures and salinity of the ore-forming stage vary from 219 to 328 °C and from 0.18 to 7.86 wt% NaCl equivalent, respectively (Yu et al. 2018). The δD, $\delta^{18}O$, and $\delta^{34}S$ values from quartz-sulfide ores range from -98 ‰ to -77 ‰, +4.8 ‰ to +8.6 ‰, and +1.1‰ to +2.4‰, respectively, interpreted to represent magmatic fluid and sulfur sources (Liu et al. 2019).

3. Analytical methods

3.1 Sample selection

In order to investigate the evolution of Fe isotopes during mineralization and its potential relationship with spatial distribution, samples of auriferous quartz-sulfide ores were collected from the No. 163 vein at depths of -516 m, -636 m, and -756 m in the underground mine. Samples thus encompass a vertical extent of about 240 m. Most samples were collected from the thick (~1m) quartz-sulfide vein, which is composed of quartz-pyrite-pyrrhotite assemblage (Fig. 4c and d). Some pyrite and pyrrhotite in the fine (~1cm) quartz-sulfide veins (Fig.4b) and

158 disseminated pyrite in the diorite (Fig.4a) were also sampled for comparison. Sample locations
159 and descriptions are given in Table 1 and illustrated in Fig. 2b.
160
161 **3.2 LA-ICP-MS quartz trace-element analyses**
162 Previous laser ablation inductively coupled plasma mass spectrometry (LA-ICP-MS)
163 studies have shown that most natural quartz grains contain measureable amounts of Fe (Audétat
164 et al. 2015). In order to evaluate the content of Fe in quartz, grains from two samples (WL18-85
165 and WL18-86, same samples analyzed for Fe isotopes) were analyzed by LA-ICP-MS for trace
166 element concentrations. The LA-ICP-MS analyses of trace elements in quartz were conducted
167 with a Geolas Pro 193 nm laser system coupled with an Agilent 7900 ICP-MS at the State Key
168 Laboratory of Ore Deposit Geochemistry, Chinese Academy of Sciences. Helium was used as
169 the carrier gas and mixed with argon before entering the torch. Laser energy was set at 10 J/cm^2,
170 and laser repetition rate was 10 Hz. A uniform spot diameter of 44 μm was used during the
171 experiment. Thirty seconds of background signal and 60 seconds of ablation were collected for
172 each analysis. Detailed analysis procedure was described in Lan et al. (2017). NIST 610 was
173 used as the external standard, and a natural quartz standard (Shandong province, China; Audétat
174 et al. 2015) was used as a secondary standard.
175
176 **3.3 Fe isotope analysis**
177 Pyrite, pyrrhotite, and quartz grains were separated by hand-picking under a binocular
178 microscope. Pyrrhotite grains were separated from pyrite magnetically. Twenty sulfides (pyrite
179 and pyrrhotite) and two quartz separates were selected for Fe isotope analyses. In particular,
180 quartz separates were carefully double-checked to avoid any possible micro grains of sulfide

inclusions. The mineral samples were cleaned ultrasonically in purified Milli-Q H_2O (18.2 MΩcm) before digestion to avoid surface contamination.

Dissolution and purification processes were carried out at the University of Science and Technology of China. Quartz grains were ground to 200 mesh to facilitate later digestion. Ultrapure HNO_3+HF (3:1) was used to digest sulfides and HNO_3+HF (1:2) was used to digest quartz. The sampling amount was around 10 mg for sulfides and 250 mg for quartz. Iron was then separated using AG1-X8 anion resin in an HCl medium. Samples were loaded and washed with 4 mL 6M HCl to remove ions other than Fe and Zn, then 4 mL 0.4M HCl, 1mL 8M HNO_3 and 0.5 mL H_2O were used to strip Fe. Iron yield was close to 100%, and the total procedural blanks were less than 10 ng.

The purified solutions were then measured for Fe isotopes on a Thermo Scientific Neptune Plus multiple collector plasma source mass spectrometer at the Hefei University of Technology, China. Instrumental mass fractionation was corrected using standard-sample bracketing, using IRMM-014 as the certified reference material. Each sample was run a minimum of 3 times. A standard was inserted after every 14 samples. To avoid molecular interferences on Fe isotopes, sample and standard concentrations were matched at 2.0 ± 0.2 ppm. Nickel and Cr are routinely monitored for both samples and standards and in no case significant contribution has been found. Three USGS reference rocks were processed with each batch of column chemistry: AGV-2, G-2, and GSP-2 (Raczek et al. 2003; Telus et al. 2012).

All data are reported using delta notation, in units of per mil relative to reference material IRMM-014, $\delta^{x}Fe = [(^{x}Fe/^{54}Fe)_{sample}/(^{x}Fe/^{54}Fe)_{IRMM\text{-}014} - 1] * 1000$ (‰), where x is either 56 or 57. The measured AGV-2 and GSP-2 standards yield $\delta^{56}Fe$ values of +0.12 ± 0.03‰ (n = 9) and +0.15 ± 0.05‰ (n = 6), consistent with their previous published values (Craddock and Dauphas

2011). The measured G-2 standard yields δ^{56}Fe values of +0.15 ± 0.05‰ (n = 9). Our data plot along a line which has a slope close to that of the theoretical mass-dependent fractionation of 1.4741 (Fig. 5), suggesting that spectral interferences have effectively been resolved in medium resolution mode.

3.4 In situ sulfur isotope analysis

In situ sulfur isotope analyses were carried out on sulfides from polished sections using a Nu Plasma II MC-ICP-MS system, equipped with a RESOlution S-155 193 nm ArF excimer laser at China University of Geosciences, Wuhan. A uniform spot diameter of 33 μm was used during the experiment, and the ablation process was set to last for 40 s at 10Hz. An in-house pyrite standard WS-1, consisting of natural pyrite crystals from the Wenshan polymetallic skarn deposit in SW China, was used to calibrate the mass bias for S isotopes. The sulfur isotope ratio of unknown samples was calculated by correction for instrumental mass bias by linear interpolation between the biases calculated from two neighboring standard analyses. All data are reported using delta notation, in units of per mil relative to reference material VCDT, $\delta^{34}S = [(^{34}S/^{32}S)_{sample}/(^{34}S/^{32}S)_{VCDT} - 1] * 1000$ (‰). The 2σ analytical precision was about ± 0.3‰.

4. Results

4.1 Iron content of quartz

The Fe contents of quartz from the quartz-sulfide veins are presented in Supplementary Table 1. Sample WL18-85 has Fe contents vary from 0.55 to 9.96 ppm with an average of 3.52 ppm, and sample WL18-86 has Fe contents vary from 0.23 to 6.95 ppm with an average of 2.25

ppm. These results are consistent with Fe concentrations of the natural quartz standard with an average content of 2.2 ppm (Audétat et al. 2015).

4.2 Fe isotopes

Iron isotope data for minerals and rock standards are presented in Table 1 and Fig. 5. Pyrites and pyrrhotites in the thick auriferous quartz-pyrite-pyrrhotite vein show a wide range in δ^{56}Fe values, varying between +0.11 ± 0.03‰ and +0.78 ± 0.03‰, and -0.85 ± 0.01‰ and -0.07 ± 0.00‰, respectively. Two quartz separates in the thick quartz-sulfide vein yield δ^{56}Fe values of -0.02 ± 0.02‰ and +0.07 ± 0.07‰, respectively. Three pyrites in the fine quartz-pyrrhotite-pyrite veins (~1cm; Fig.4d) yield δ^{56}Fe values vary between +0.35 ± 0.02‰ and +0.40 ± 0.01‰, and pyrrhotites from the same veins are isotopically lighter than the pyrite, varying between -0.55 ± 0.01‰ and -0.51 ± 0.07‰. Two disseminated pyrites in diorite yield δ^{56}Fe values of +0.38 ± 0.02‰ to +0.41 ± 0.03‰. The δ^{56}Fe values of sulfides in fine quartz-sulfide veins and diorite are consistent with those in the thick auriferous quartz-sulfide vein. The average δ^{56}Fe values of sulfides from -756m, -636m, to -516m are -0.33 (n=6), -0.08 (n=6), and 0.14 (n=8), respectively. They generally become heavier upward.

4.3 Sulfur isotopes of pyrite and pyrrhotite

Forty-five in situ sulfur isotope compositions of sulfides (22 pyrites and 23 pyrrhotites) were determined in 10 samples from the Wulong ores. The sulfur isotopic data are listed in Table 2 and plotted in Fig. 6. The δ^{34}S values of the sulfides range from -1.2‰ to +4.1‰. On average, pyrite (δ^{34}S ranging from +0.5 to +4.1‰) is isotopically heavier than pyrrhotite (-1.2 to +1.2‰).

5. Discussion

5.1 Fe isotope fractionation in the Wulong deposit

In the Wulong deposit, quartz-sulfide veins are the predominant ores, and pyrite and pyrrhotite are the main Fe-bearing minerals (Fig.3 and 4). The Fe isotopic composition of minerals can be used to evaluate evolution of fluids in hydrothermal environments with available fractionation factors of Fe-bearing minerals and ferrous fluids (Polyakov and Soultanov 2011; Dauphas et al. 2017). Equilibrium fractionation between phases is usually expressed using the α notation (1),

$$\Delta_{A-B} = \delta^{56}Fe_A - \delta^{56}Fe_B \approx 10^3 \ln \alpha^{56}Fe_{A-B} \quad (1)$$

where the subscripts A and B are two phases. The fractionation factors can be related to the reduced partition function ratio β-factor through (2),

$$10^3 \ln \alpha^{56}Fe_{A-B} = 10^3 \ln \beta_A - 10^3 \ln \beta_B \quad (2)$$

The β is the equilibrium fractionation factor between a given phase and the reference state of monoatomic vapor Fe (Dauphas et al. 2017). Theoretical Fe fractionation factors are calculated using the equations (1) and (2). Experimental studies have shown that Fe is mainly present as Fe^{2+}_{aq} in magmatic-hydrothermal fluids (Chou and Eugster 1977; Simon et al. 2004). We adopted the most recent reduced partition functions of Fe^{2+}_{aq} from Rustad and Dixon (2009) and pyrite from Blanchard et al. (2009) to calculate fluid (Fe^{2+}_{aq}) and pyrite fractionation factors. Pyrrhotite and troilite are all members of the same $Fe_{1-x}S$ (x = 0-0.125) mineral group, and they only have a slight distortion difference in the ideal NiAs crystal structure. Schuessler et al. (2007) proposed that β-factor for troilite can be used for pyrrhotite, and it has been applied in hydrothermal ore-forming systems (Wawryk and Foden 2015; Li et al. 2018). Therefore, troilite from Polyakov et al. (2007) is used to calculate pyrrhotite fractionation factors in this study.

At a given temperature, it can be predicted that $10^3 \ln \beta$pyrite > βmagnetite > βFe^{2+}_{aq} > βpyrrhotite (Fig.7a; Polyakov and Soultanov 2011; Dauphas et al. 2017). Thus, pyrite should be isotopically heavier than cogenetic pyrrhotite. Our data are consistent with the theoretical predictions of equilibrium fractionation that pyrite is isotopically heavier than pyrrhotite, indicating that equilibrium fractionation has been reached. The results of this study are consistent with those reported by Wawryk and Foden (2015) as well as Wang et al. (2015) who also reported pyrite to be isotopically heavier than pyrrhotite.

5.2 Ore-forming processes

Quartz, pyrite, and pyrrhotite are the main minerals in the Wulong ores (Fig.4). Although minor chalcopyrite grains (<0.1%) also occur in the Wulong deposit, they have little influence on the Fe isotopic composition of the system due to their low abundance.

Previous study has shown that fluid inclusion homogenization temperatures of the main ore-forming stage in the Wulong deposit reach a peak between 280 and 300°C (Yu et al. 2018). This temperature range is consistent with our analyses (unpublished data) of fluid inclusions in the quartz veins that contain pyrite and pyrrhotite. We use 300°C as the temperature for fractionation factor calculation of Fe isotopes in pyrite- pyrrhotite - Fe^{2+}_{aq} system (Fig.8). At 300°C, using the fractionation factors of Fe^{2+}_{aq} (Rustad and Dixon 2009), pyrite (Blanchard et al. 2009), and pyrrhotite (Polyakov et al. 2007), the calculated fractionation factor is 1.09‰ between pyrite and fluid, and between pyrrhotite and fluid is -0.52‰. The heaviest and lightest δ^{56}Fe values for pyrite and pyrrhotite are +0.78‰ and -0.85‰, respectively. The calculation results show that the initial δ^{56}Fe value for the ore-forming fluid is -0.31‰ assuming only pyrite is the main Fe-bearing minerals in the system, and initial δ^{56}Fe value for the ore-forming fluid is -0.33‰

assuming only pyrrhotite is the main Fe-bearing minerals in the system. The agreement between these values suggests the calculations yield a well-constrained value for initial fluid δ^{56}Fe, especially considering consistency with values from hydrothermal fluids in hot springs (Sharma et al. 2001). The δ^{56}Fe values of pyrite and pyrrhotite are plotted in the pyrite and pyrrhotite evolution lines (Fig.8).

Pyrite and pyrrhotite have different oxygen fugacity stability fields under hydrothermal conditions (Cooke et al. 1996; Wawryk and Foden 2017). Theoretical Fe isotope fractionation between minerals and an Fe^{2+}-bearing fluid suggests that pyrite will be isotopically heavier than the fluid and pyrrhotite will be lighter (Fig. 7b). In addition, based on the following lines of evidence, we consider that δ^{56}Fe values of quartz can represent the Fe isotopes of ore-forming fluids during pyrite and pyrrhotite precipitation. Considering that quartz crystallized directly from the same fluid that produced the ore minerals, we consider that δ^{56}Fe values of quartz effectively represents the Fe isotopes of ore-forming fluids during pyrite and pyrrhotite precipitation. Prior studies have used isotopic compositions of quartz in a similar fashion (Goldfarb et al. 1991; Shanks 2014). Thus, the Fe isotopic compositions of pyrite, pyrrhotite, and quartz can be used to trace the evolution of oxygen fugacity during ore-forming processes.

In the case of the Wulong gold deposit, three possibilities appear to exist for the sequence of crystallization of sulfides: (1) pyrite crystallized first, (2) pyrite and pyrrhotite co-crystallized, and (3) pyrrhotite crystallized first. The petrographic relations between pyrite and pyrrhotite are ambiguous (Fig. 4e and f). Assuming that pyrite crystallized first, the δ^{56}Fe of the initial ore-forming fluid would be -0.31‰ and would gradually decrease as precipitation of pyrite proceeds (Fig.8a). This result is consistent with experimental study of Fe isotopic fractionation between pyrite and Fe^{2+}_{aq} under hydrothermal conditions (Syverson et al. 2013). However, the calculated

318 δ^{56}Fe of the remaining fluids would be much lower than quartz separates in the quartz-sulfide
319 ores (-0.02‰ and +0.07‰), suggesting that pyrite did not crystallize before pyrrhotite. Similarly,
320 if pyrite and pyrrhotite co-crystallized, δ^{56}Fe values of ore-forming fluids would be lower than
321 quartz separates in the quartz-sulfide ores (Fig. 8b). Assuming the pyrrhotite crystallized first,
322 the δ^{56}Fe values of ore-forming fluids are consistent with those of quartz separates (Fig. 8c).
323 Thus we interpret that pyrrhotite crystallized before pyrite in the Wulong deposit, indicating a
324 relatively low oxygen fugacity environment at the early stage of ore formation. The subsequent
325 precipitation of pyrite records an increase of oxygen fugacity during mineralization. In addition,
326 the degree of oxygen fugacity increase is limited because chalcopyrite is the only Cu-bearing
327 mineral and no bornite was observed in the Wulong deposit (Fig.9). It is noteworthy that pyrite
328 exerts a greater impact on the evolution of Fe isotopes than pyrrhotite during the mineralization
329 processes (Fig.7). Thus, initial precipitation dominated by pyrrhotite with slightly positive δ^{56}Fe
330 values of ore-forming fluids would give way to Fe isotopic effects of subsequent pyrite
331 precipitation, resulting in evolution of Fe isotopes towards negative values.

332 Based on the geological observations and isotopic data in this study, ore-forming processes
333 of the Wulong deposit can be summarized as follows. Pyrrhotite (low δ^{56}Fe) crystallized first
334 from the initial ore-forming fluids under a relatively low oxygen fugacity conditions, resulting in
335 increase in δ^{56}Fe of the remaining ore-forming fluids. Due to increasing oxygen fugacity,
336 perhaps from addition of meteoric water, ore fluids subsequently crystallize pyrite (high δ^{56}Fe).
337 The addition of meteoric waters is supported by decreases of temperatures and $\delta^{18}O_{fluid}$ values
338 during the ore-forming processes in the Wulong deposit (Yu et al. 2018).
339

340 **5.3 Comparison with Fe isotopic compositions in Wulong and other gold deposits**

The Jiaodong Peninsula is China's principal source for gold and is one of the globally important gold provinces. The Wulong deposit is adjacent to the Jiaodong gold province, and they share many similar geological characteristics (Goldfarb and Santosh 2014; Zhu et al. 2015; Yu et al. 2018) including: (1) Gold orebodies are hosted in Mesozoic granites; (2) Gold mineralization occurred at ca. 120 Ma; (3) Major ore minerals precipitated at ca. 300℃. However, unlike most gold deposits in Jiaodong, which are dominated by pyrite, Wulong gold deposit contains a large amount of pyrrhotite and pyrite, indicating that it was formed under more reducing conditions (Fig. 9).

Pyrites from the Wulong deposit have a relatively wide range of δ^{56}Fe values (0.11‰ to 0.78‰). By contrast, the δ^{56}Fe values of pyrite from quartz-sulfide veins in the Jiaodong gold deposits show a much larger range, varying from -0.78‰ and +0.79‰ (Zhu et al. 2018). In addition to Fe isotopes, pyrites from Jiaodong gold deposits have systematically heavier sulfur isotopes (δ^{34}S +6.8 to +12.5‰; Mao et al. 2008) than those from the Wulong gold deposit (+0.5‰ to +4.1 ‰). In Figure 10, δ^{56}Fe from individual pyrite grains are plotted against average δ^{34}S from in situ measurements from the same grains. No correlation is apparent between the two isotope systems. The possible reason for the differences in Fe isotopes is that under low oxygen fugacity conditions, pyrrhotite from the Wulong deposit with light Fe isotopes crystallized first from the ore-forming fluids, and the remaining fluids with heavy Fe isotopes can only precipitate pyrites with positive δ^{56}Fe values. The distinct δ^{34}S values between the Wulong and Jiaodong deposits may be accounted for their different source regions or oxygen fugacities. It has been shown that hydrothermal pyrites formed under higher oxygen fugacities would yield 3.5 to 5.4‰ lower δ^{34}S values (Cai et al. 2018; Zhu et al. 2018), which is inconsistent with the Wulong and Jiaodong data. Therefore, the difference in oxygen fugacities alone is not a plausible explanation

here, and the differences in $\delta^{34}S$ between Wulong and the Jiaodong deposits must reflect differences in sources of sulfur.

Porphyry Cu-Au deposits are also major gold resources, and Fe isotope data exist for some. Pyrite from the Duolong porphyry Cu-Au deposit has $\delta^{56}Fe$ ranging from +0.23 to +0.48‰ (Li et al. 2018), within the range for Wulong pyrite. However, the Wulong gold deposit records an increase of oxygen fugacity during mineralization, which is different from the porphyry Cu-Au deposits that are characterized by a decrease of oxygen fugacity during ore formation (Fig.9).

5.4 Fe isotopic compositions of pyrite and pyrrhotite in various ore deposits

Pyrite and pyrrhotite are common minerals in magmatic and hydrothermal ore-forming systems, and their Fe isotopic compositions provide a valuable means for understanding mineralization processes. We have compiled $\delta^{56}Fe$ values from pyrite and pyrrhotite in porphyry deposits (Li et al. 2018), skarn deposits (Wang et al. 2011, 2015), porphyry-skarn deposits (Graham et al. 2004), hydrothermal W-Sn deposits (Wawryk and Foden 2015), orogenic gold deposits (Zhu et al. 2018), and magmatic Ni-Cu deposits (Bilenker et al. 2018; Ding et al. 2019) to compare Fe isotopes vary in different ore-forming environments.

Pyrite from the assembled ore deposit data set spans a wide δ56Fe range of ~4‰ (Fig. 11a). Nevertheless, there are some systematic differences among different deposit types. (1) Pyrites from high temperature hydrothermal W-Sn and porphyry deposits show a narrow range of positive $\delta^{56}Fe$ values (Wawryk and Foden 2015; Li et al. 2018). This is consistent with equilibrium fractionation since pyrite has the highest ln β values among common ore minerals (Fig.7a). (2) Pyrites from porphyry-skarn (Grasberg, Mathur et al. 2000; Pollard et al. 2005) and skarn deposits have a wide range of $\delta^{56}Fe$ values, both positive and negative (Graham et al. 2004;

Wang et al. 2011, 2015). Negative δ^{56}Fe values of pyrites in the skarn systems may be due to a mixture between magmatic and sedimentary sources (Graham et al. 2004). (3) Pyrites from Jiaodong and Wulong gold deposits show both positive and negative δ^{56}Fe values, and the negative values were explained by Rayleigh fractionation during pyrite precipitation in an open system (Zhu et al. 2018). In general, positive pyrite δ^{56}Fe values reflect an equilibrium isotope effect, whereas negative pyrite δ^{56}Fe values may be due to a kinetic isotope effects or a mixture of sedimentary host rocks (Graham et al. 2004; Mansor and Fantle 2019).

Unlike pyrite, pyrrhotite grains from different types of ore deposits show similar narrow ranges of δ^{56}Fe values (Fig.11b). Most pyrrhotites from these deposits show negative δ^{56}Fe values, ranging between -1.0 and 0.0‰, with a minority of slightly positive values from skarn and magmatic Ni-Cu deposits (Wang et al. 2015; Wawryk and Foden 2015; Bilenker et al. 2018; Ding et al. 2019). It has been proposed that magmatic assimilation of country rocks may explain the isotopically light and heavy nature of pyrrhotites (Bilenker et al. 2018). However, pyrrhotites from hydrothermal skarn deposit with sedimentary host rocks show no more significant shift toward negative δ^{56}Fe values than with other deposits. In addition, pyrrhotites from the Wulong hydrothermal gold deposit with host igneous rocks having positive δ^{56}Fe values do not show an obvious shift toward more positive δ^{56}Fe. Therefore, the effect of contamination on the Fe isotopic compositions of hydrothermal pyrrhotite may be limited.

Mass balance is the primary control on Fe isotopes in a defined geological system. As such, the variations in the crystallization history of Fe-bearing minerals controls the Fe isotopic composition of that system. Among the common Fe-bearing ore minerals in magmatic-hydrothermal systems, pyrite and pyrrhotite have the highest and lowest β-factors, respectively (Fig.7a; Dauphas et al. 2017). Hence, under equilibrium conditions, pyrite will favorably

incorporate heavier Fe than will pyrrhotite. However, although pyrrhotite from various types of deposits always shows light Fe isotopes, the δ^{56}Fe values of pyrite vary significantly with the presence or absence of pyrrhotite (Fig.11). This may be due to the preference of pyrrhotite for isotopically light Fe, which strongly influences the Fe isotopic systems in magmatic-hydrothermal porphyry deposits (Wawryk and Foden 2017; Li et al. 2018). Similar Fe isotopic patterns of pyrrhotite have also been reported in magmatic systems (Schuessler et al. 2007; Bilenker et al. 2018).

6. Implications

Pyrite and pyrrhotite are the major Fe-bearing minerals of the quartz-sulfide veins in the Wulong reduced gold deposit. Iron isotope fractionation modeling shows that under a relatively low oxygen fugacity condition, pyrrhotite with low δ^{56}Fe crystallized first from the initial ore-forming fluids, resulting in fluids with elevated δ^{56}Fe values. Due to an increase of oxygen fugacity, pyrite with heavy δ^{56}Fe values started to precipitate later. The Fe isotopic compositions provide a new perspective for the initial redox condition and evolution of the Wulong gold deposit, which are important to trace the source of ore-forming materials and further exploration.

Most pyrrhotite grains from different types of ore deposits show similar distribution of negative δ^{56}Fe values, and the effect of contamination on Fe isotope composition of pyrrhotite may be limited at Wulong. Pyrrhotite exerts a strong control on the Fe isotope systematics in magmatic and hydrothermal environments. The Fe isotopic compositions of other sulfides during the ore forming processes of gold mineralization and their controlling factors are an interesting topic in the future research.

Acknowledgements

We thank Haicheng Qiu and Fuxing Liu for providing assistance during our field investigations. We are grateful to Dr. Ryan Mathur and anonymous reviewer(s) who made constructive comments and helped to improve the language on an early version of our manuscript. Associate Editor Paul Tomascak is especially thanked for the editorial handling, helpful suggestions, and language polishing.

Funding

This research was supported by the National Key Research and Development Program of China (2018YFC0603801) and National Natural Science Foundation of China (Nos. 41903042 and 41530206).

References cited

Audétat, A., Garbe‐Schönberg, D., Kronz, A., Pettke, T., Rusk, B., Donovan, J. J., and Lowers, H. A. (2015) Characterisation of a natural quartz crystal as a reference material for microanalytical determination of Ti, Al, Li, Fe, Mn, Ga and Ge. Geostandards and Geoanalytical Research, 39(2), 171-184.

Bilenker, L. D., Simon, A. C., Reich, M., Lundstrom, C. C., Gajos N., Bindeman, I., Barra, F., and Munizaga, R. (2016) Fe–O stable isotope pairs elucidate a high-temperature origin of Chilean iron oxide-apatite deposits. Geochimica et Cosmochimica Acta 177, 94-104.

Bilenker, L. D., VanTongeren, J. A., Lundstrom, C. C., and Simon, A. C. (2017) Iron isotopic evolution during fractional crystallization of the uppermost B ushveld C omplex layered mafic intrusion. Geochemistry, Geophysics, Geosystems, 18(3), 956-972.

456 Bilenker, L. D., Weis, D., Scoates, J. S. and Perry, E. (2018) The application of stable Fe
457 isotopes to magmatic sulfide systems: Constraints on the Fe isotope composition of
458 magmatic pyrrhotite. Economic Geology, 113(5), 1181-1192.
459 Blanchard, M., Poitrasson, F., Meheut, M., Lazzeri, M., Mauri, F., and Balan E. (2009) Iron
460 isotope fractionation between pyrite (FeS_2), hematite (Fe_2O_3) and siderite ($FeCO_3$): a first-
461 principles density functional theory study. Geochimica et Cosmochimica Acta, 73(21),
462 6565-6578.
463 Cai, Y. C., Fan, H. R., Santosh, M., Hu, F. F., Yang, K. F., and Li X. H. (2018) Decratonic gold
464 mineralization: evidence from the Shangzhuang gold deposit, eastern North China Craton.
465 Gondwana Research, 54, 1-22.
466 Chang, Z.S., Large, R. R., and Maslennikov, V. (2008) Sulfur isotopes in sediment-hosted
467 orogenic gold deposits: Evidence for an early timing and a seawater sulfur source. Geology,
468 36(12), 971-974.
469 Childress, T. M., Simon, A. C., Day, W. C., Lundstrom, C. C., and Bindeman, I. N. (2016) Iron
470 and oxygen isotope signatures of the Pea Ridge and Pilot Knob magnetite-apatite deposits,
471 southeast Missouri, USA. Economic Geology, 111(8), 2033-2044.
472 Chou, I. M. and Eugster, H. P. (1977) Solubility of magnetite in supercritical chloride solutions.
473 American Journal of Science, 277(10), 1296-1314.
474 Cooke, D. R., McPhail, D. C. and Bloom, M. S. (1996) Epithermal gold mineralization, Acupan,
475 Baguio District, Philippines; geology, mineralization, alteration, and the thermochemical
476 environment of ore deposition. Economic Geology, 91(2), 243-272.
477 Craddock, P. R. and Dauphas, N. (2011) Iron and carbon isotope evidence for microbial iron
478 respiration throughout the Archean. Earth and Planetary Science Letters, 303(1-2), 121-132.

Dauphas, N., Craddock, P. R., Asimow, P. D., Bennett, V. C., Nutman, A. P., and Ohnenstetter, D. (2009) Iron isotopes may reveal the redox conditions of mantle melting from Archean to Present. Earth and Planetary Science Letters, 288(1-2), 255-267.

Dauphas, N., Roskosz, M., Alp, E. E., Neuville, D. R., Hu, M. Y., Sio, C. K., Tissot, F.L.H., Zhao, J., Tissandier, L., Médard, E., and Cordier, C. (2014) Magma redox and structural controls on iron isotope variations in Earth's mantle and crust. Earth and Planetary Science Letters, 398, 127-140.

Dauphas, N., John, S. G., and Rouxel, O. (2017) Iron isotope systematics. Reviews in Mineralogy and Geochemistry, 82(1), 415-510.

Ding, X., Ripley, E. M., Wang, W., Li, C., and Huang, F. (2019) Iron isotope fractionation during sulfide liquid segregation and crystallization at the Lengshuiqing Ni-Cu magmatic sulfide deposit, SW China. Geochimica et Cosmochimica Acta, 261, 327-341.

Foden, J., Sossi, P. A. and Wawryk, C. M. (2015) Fe isotopes and the contrasting petrogenesis of A-, I-and S-type granite. Lithos, 212, 32-44.

Goldfarb, R. J., Newberry, R. J., Pickthorn, W. J. and Gent, C. A. (1991) Oxygen, hydrogen, and sulfur isotope studies in the Juneau gold belt, southeastern Alaska; constraints on the origin of hydrothermal fluids. Economic Geology, 86(1), 66-80.

Goldfarb, R. J. and Santosh, M. (2014) The dilemma of the Jiaodong gold deposits: are they unique? Geoscience Frontiers, 5(2), 139-153.

Graham, S., Pearson, N., Jackson, S., Griffin, W., and O'reilly, S. Y. (2004) Tracing Cu and Fe from source to porphyry: in situ determination of Cu and Fe isotope ratios in sulfides from the Grasberg Cu–Au deposit. Chemical Geology, 207(3-4), 147-169.

501 Johnson, C. M., Beard, B. L., Beukes, N. J., Klein, C., and O'Leary, J. M. (2003) Ancient
502 geochemical cycling in the Earth as inferred from Fe isotope studies of banded iron
503 formations from the Transvaal Craton. Contributions to Mineralogy and Petrology, 144(5),
504 523-547.
505 Johnson, C. M., Beard, B. L., Klein, C., Beukes, N. J., and Roden, E. E. (2008) Iron isotopes
506 constrain biologic and abiologic processes in banded iron formation genesis. Geochimica et
507 Cosmochimica Acta, 72(1), 151-169.
508 Knipping, J. L., Bilenker, L. D., Simon, A. C., Reich, M., Barra, F., Deditius, A. P., Lundstrom,
509 C., Bindeman, I., and Munizaga, R. (2015) Giant Kiruna-type deposits form by efficient
510 flotation of magmatic magnetite suspensions. Geology, 43(7), 591-594.
511 Knipping, J. L., Fiege, A., Simon, A. C., Oeser, M., Reich, M., and Bilenker, L. D. (2019) In-situ
512 iron isotope analyses reveal igneous and magmatic-hydrothermal growth of magnetite at the
513 Los Colorados Kiruna-type iron oxide-apatite deposit, Chile. American Mineralogist, 104(4),
514 471-484.
515 Lan, T.G., Hu, R.Z., Fan, H.R., Bi, X.W., Tang, Y.W., Zhou, L., Mao, W., and Chen, Y.H.,
516 (2017) In-situ analysis of major and trace elements in fluid inclusion and quartz: LA-ICP-
517 MS method and applications to ore deposits. Acta Petrologica Sinica, 33 (10), 3239–3262.
518 Li, J. X., Qin, K. Z., Li, G. M., Evans, N. J., Huang, F., and Zhao, J. X. (2018) Iron isotope
519 fractionation during magmatic-hydrothermal evolution: A case study from the Duolong
520 porphyry Cu-Au deposit, Tibet. Geochimica et Cosmochimica Acta, 238, 1-15.
521 Liu, J., Zhang, L.J., Wang, S.L., Li, T.G., Yang, Y, Liu, F.X., Li, S.H., and Duan, C. (2019)
522 Formation of the Wulong gold deposit, Liaodong gold Province, NE China: Constraints

523 from zircon U–Pb age, sericite Ar–Ar age, and H–O–S–He isotopes, Ore Geology Reviews,
524 109, 130-143.
525 Mansor, M., and Fantle, M. S. (2019) A novel framework for interpreting pyrite-based Fe isotope
526 records of the past. Geochimica et Cosmochimica Acta, 253, 39-62.
527 Mao, J.W., Wang, Y.T., Li, H.M., Pirajno, F., Zhang, C., and Wang, R. (2008) The relationship
528 of mantle-derived fluids to gold metallogenesis in the Jiaodong Peninsula: evidence from D–
529 O–C–S isotope systematics. Ore Geology Reviews, 33(3-4), 361-381.
530 Markl, G., Von Blanckenburg, F., and Wagner, T. (2006) Iron isotope fractionation during
531 hydrothermal ore deposition and alteration. Geochimica et Cosmochimica Acta, 70(12),
532 3011-3030.
533 Mathur, R., Ruiz, J., Titley, S., Gibbins, S., and Margotomo, W. (2000) Different crustal sources
534 for Au-rich and Au-poor ores of the Grasberg Cu–Au porphyry deposit. Earth and Planetary
535 Science Letters, 183(1-2), 7-14.
536 Mathur, R., and Wang, D. (2019) Transition Metal Isotopes Applied to Exploration
537 Geochemistry: Insights from Fe, Cu, and Zn. in Decrée, S., and Robb, L., eds., Ore Deposits:
538 Origin, Exploration, and Exploitation: Washington, American Geophysical Union, 163-183.
539 Meinert, L. D., Hedenquist, J. W., Satoh, H., and Matsuhisa, Y. (2003) Formation of anhydrous
540 and hydrous skarn in Cu-Au ore deposits by magmatic fluids. Economic Geology, 98(1),
541 147-156.
542 Mikhlin, Y., and Tomashevich, Y. (2005) Pristine and reacted surfaces of pyrrhotite and
543 arsenopyrite as studied by X-ray absorption near-edge structure spectroscopy. Physics and
544 Chemistry of Minerals, 32(1), 19-27.

Pollard, P. J., Taylor, R. G., and Peters, L. (2005) Ages of intrusion, alteration, and mineralization at the Grasberg Cu-Au deposit, Papua, Indonesia. Economic Geology, 100(5), 1005-1020.

Polyakov, V. B., Clayton, R. N., Horita, J., and Mineev S. D. (2007) Equilibrium iron isotope fractionation factors of minerals: reevaluation from the data of nuclear inelastic resonant X-ray scattering and Mössbauer spectroscopy. Geochimica et Cosmochimica Acta, 71(15), 3833-3846.

Polyakov, V. B., and Soultanov, D. M. (2011) New data on equilibrium iron isotope fractionation among sulfides: Constraints on mechanisms of sulfide formation in hydrothermal and igneous systems. Geochimica et Cosmochimica Acta, 75(7), 1957-1974.

Raczek, I., Jochum, K. P., and Hofmann, A. W. (2003) Neodymium and strontium isotope data for USGS reference materials BCR-1, BCR-2, BHVO-1, BHVO-2, AGV-1, AGV-2, GSP-1, GSP-2 and eight MPI-DING reference glasses. Geostandards Newsletter, 27(2), 173-179.

Rouxel, O., Shanks, III W. C., Bach, W., and Edwards, K. J. (2008) Integrated Fe-and S-isotope study of seafloor hydrothermal vents at East Pacific Rise 9–10 N. Chemical Geology, 252(3-4), 214-227.

Rustad, J. R., and Dixon, D. A. (2009) Prediction of iron-isotope fractionation between hematite (α-Fe2O3) and ferric and ferrous iron in aqueous solution from density functional theory. The Journal of Physical Chemistry A, 113(44), 12249-12255.

Schauble, E. A., Rossman, G. R., and Taylor Jr, H. P. (2001) Theoretical estimates of equilibrium Fe-isotope fractionations from vibrational spectroscopy. Geochimica et Cosmochimica Acta, 65(15), 2487-2497.

567 Schuessler, J. A., Schoenberg, R., Behrens, H., and von Blanckenburg, F. (2007) The
568 experimental calibration of the iron isotope fractionation factor between pyrrhotite and
569 peralkaline rhyolitic melt. Geochimica et Cosmochimica Acta, 71(2), 417-433.
570 Schoenberg, R., Marks, M. A., Schuessler, J. A., von Blanckenburg, F., and Markl, G. (2009) Fe
571 isotope systematics of coexisting amphibole and pyroxene in the alkaline igneous rock suite
572 of the Ilímaussaq Complex, South Greenland. Chemical Geology, 258(1-2), 65-77.
573 Shanks, W.C. (2014) Stable isotope geochemistry of mineral deposits. Treatise on Geochemistry,
574 2nd ed. Elsevier, Oxford, 59-85.
575 Sharma, M., Polizzotto, M., and Anbar, A. D. (2001) Iron isotopes in hot springs along the Juan
576 de Fuca Ridge. Earth and Planetary Science Letters, 194(1-2), 39-51.
577 Simon, A. C., Pettke, T., Candela, P. A., Piccoli, P. M., and Heinrich, C. A. (2004) Magnetite
578 solubility and iron transport in magmatic-hydrothermal environments. Geochimica et
579 Cosmochimica Acta, 68(23), 4905-4914.
580 Sossi, P. A., Foden J. D., and Halverson G. P. (2012) Redox-controlled iron isotope fractionation
581 during magmatic differentiation: an example from the Red Hill intrusion, S. Tasmania.
582 Contributions to Mineralogy and Petrology, 164(5), 757-772.
583 Steinhoefel, G., von Blanckenburg, F., Horn, I., Konhauser, K. O., Beukes N. J., and Gutzmer, J.
584 (2010) Deciphering formation processes of banded iron formations from the Transvaal and
585 the Hamersley successions by combined Si and Fe isotope analysis using UV femtosecond
586 laser ablation. Geochimica et Cosmochimica Acta, 74(9), 2677-2696.
587 Syverson, D. D., Borrok, D. M., and Seyfried, Jr W. E. (2013) Experimental determination of
588 equilibrium Fe isotopic fractionation between pyrite and dissolved Fe under hydrothermal
589 conditions. Geochimica et Cosmochimica Acta, 122, 170-183.

590 Telus, M., Dauphas, N., Moynier, F., Tissot, F. L., Teng, F. Z., Nabelek, P. I., Craddock, P. R.,
591 and Groat, L. A. (2012) Iron, zinc, magnesium and uranium isotopic fractionation during
592 continental crust differentiation: The tale from migmatites, granitoids, and pegmatites.
593 Geochimica et Cosmochimica Acta, 97, 247-265.
594 Troll, V. R., Weis, F. A., Jonsson, E., Andersson, U. B., Majidi, S. A., Högdahl, K., Harris, C.,
595 Millet, M.A., Chinnasamy, S.S., Kooijman, E., and Nilsson, K. P. (2019) Global Fe–O
596 isotope correlation reveals magmatic origin of Kiruna-type apatite-iron-oxide ores. Nature
597 communications, 10(1), 1712.
598 Ulrich, T., Günther, D., and Heinrich, C. A. (2002) The evolution of a porphyry Cu-Au deposit,
599 based on LA-ICP-MS analysis of fluid inclusions: Bajo de la Alumbrera, Argentina.
600 Economic Geology, 97(8), 1889-1920.
601 Wang, Y., Zhu, X. K., Mao, J. W., Li, Z. H., and Cheng, Y. B. (2011) Iron isotope fractionation
602 during skarn-type metallogeny: a case study of Xinqiao Cu–S–Fe–Au deposit in the Middle–
603 Lower Yangtze valley. Ore Geology Reviews, 43(1), 194-202.
604 Wang, Y., Zhu, X. K., and Cheng, Y.B. (2015) Fe isotope behaviours during sulfide-dominated
605 skarn-type mineralisation. Journal of Asian Earth Sciences, 103, 374-392.
606 Wawryk, C. M., and Foden J. D. (2015) Fe-isotope fractionation in magmatic-hydrothermal
607 mineral deposits: a case study from the Renison Sn–W deposit, Tasmania. Geochimica et
608 Cosmochimica Acta, 150, 285-298.
609 Wawryk, C. M., and Foden, J. D. (2017) Iron-isotope systematics from the Batu Hijau Cu-Au
610 deposit, Sumbawa, Indonesia. Chemical Geology, 466, 159-172.

611 Wan, Y. S., Liu, S. J., Xie, H. Q., Dong, C. Y., Li, Y., Bai, W. Q., and Liu, D. Y. (2018)
612 Formation and evolution of the Archean continental crust of China: A review. China
613 Geology, 1(1), 109-136.
614 Wu, F. Y., Yang, J. H., Wilde, S. A., and Zhang X. O. (2005) Geochronology, petrogenesis and
615 tectonic implications of Jurassic granites in the Liaodong Peninsula, NE China. Chemical
616 Geology, 221(1-2), 127-156.
617 Wu, F. Y., Yang, J. H., Xu, Y. G., Wilde, S. A., and Walker, R. J. (2019) Destruction of the
618 North China Craton in the Mesozoic. Annual Review of Earth and Planetary Sciences, 47,
619 173-195.
620 Yang, J. H., Wu, F. Y., Wilde, S. A., and Liu, X. M. (2007) Petrogenesis of Late Triassic
621 granitoids and their enclaves with implications for post-collisional lithospheric thinning of
622 the Liaodong Peninsula, North China Craton. Chemical Geology, 242(1-2), 155-175.
623 Yu, B., Zeng, Q., Frimmel, H. E., Wang, Y., Guo, W., Sun, G., Zhou, T., and Li, J. (2018)
624 Genesis of the Wulong gold deposit, northeastern North China Craton: Constraints from
625 fluid inclusions, H-O-S-Pb isotopes, and pyrite trace element concentrations. Ore Geology
626 Reviews, 102, 313-337.
627 Zhang, S. H., Zhao, Y., Davis, G. A., Ye, H., and Wu, F. (2014) Temporal and spatial variations
628 of Mesozoic magmatism and deformation in the North China Craton: Implications for
629 lithospheric thinning and decratonization. Earth-Science Reviews, 131, 49-87.
630 Zhao, Y., Xue, C., Liu, S. A., Mathur, R., Zhao, X., Yang, Y., Dai, J., Man, R., and Liu, X.
631 (2019) Redox reactions control Cu and Fe isotope fractionation in a magmatic Ni–Cu
632 mineralization system. Geochimica et Cosmochimica Acta, 249, 42-58.

633 Zheng, J.H., Mao, J.W., Yang, F.Q., Chai, F.M., and Zhu, Y.F. (2017) Mineralogy, fluid
634 inclusions, and isotopes of the Cihai iron deposit, eastern Tianshan, NW China: implication
635 for hydrothermal evolution and genesis of subvolcanic rocks-hosted skarn-type deposits.
636 Ore Geology Reviews, 86, 404-425.
637 Zheng, J.H., Shen, P., and Li, C.H. (2020) Ore genesis of Axi post-collisional epithermal gold
638 deposit, western Tianshan, NW China: Constraints from U–Pb dating, Hf isotopes, and
639 pyrite in situ sulfur isotopes. Ore Geology Reviews, 117, 103290.
640 Zhu, R., Fan, H., Li, J., Meng, Q., Li, S., and Zeng, Q. (2015) Decratonic gold deposits. Science
641 China Earth Sciences, 58(9), 1523-1537.
642 Zhu, Z. Y., Jiang, S. Y., Mathur, R., Cook, N. J., Yang, T., Wang, M., Ma, L., and Ciobanu, C. L.
643 (2018) Iron isotope behavior during fluid/rock interaction in K-feldspar alteration zone–A
644 model for pyrite in gold deposits from the Jiaodong Peninsula, East China. Geochimica et
645 Cosmochimica Acta, 222, 94-116.
646 Zürcher, L., Ruiz, J., and Barton, M. D. (2001) Paragenesis, elemental distribution, and stable
647 isotopes at the Peña Colorada iron skarn, Colima, Mexico. Economic Geology, 96(3), 535-
648 557.
649
650
651
652 **Figure Captions**
653 Figure 1. (a) Simplified geological map of the North China Craton with the distribution of
654 Precambrian basement and Mesozoic intrusive rocks (modified from Zhang et al. 2014 and Wan

et al. 2018). (b) Geological map of the Liaodong Peninsula with the distribution of major gold deposits.

Figure 2. (a) Geological map of the Wulong gold ore district with the distribution of intrusive rocks and gold orebodies. (b) A underground geological map of the No.163 vein at different depths in the Wulong gold deposit.

Figure 3. Field photos showing the spatial relationship between ore bodies and magmatic rocks in the Wulong gold deposit. (a) Granite and diorite as the main host rocks of the quartz-sulfide ores, and some post-ore diabase dikes crosscut the quartz-sulfide ores. (b) A close-up view for the quartz-sulfide ore. (c) Quartz-sulfide ores contain various sizes of diorite breccia. (d) Fine quartz-sulfide veins are spatially adjacent to quartz-sulfide orebodies.

Figure 4. Representative photos and reflected light photomicrographs of samples in the Wulong deposit. (a) Disseminated pyrite in altered diorite. (b) Quartz sulfide veinlet crosscut diorite. (c) and (d) Quartz sulfide ores consist predominantly of quartz, pyrrhotite, and pyrite. (e) Pyrite, pyrrhotite, native gold, and quartz coexist in quartz sulfide ores. (f) Pyrite enclosing pyrrhotite in the ores.
Mineral abbreviations: Py = pyrite, Po = pyrrhotite, Qtz = quartz, Au = native gold.

Figure 5. Iron isotopic compositions ($\delta^{57}Fe$ vs. $\delta^{56}Fe$) of all samples analyzed in the Wulong gold deposit.

678 Figure 6. In situ sulfur isotope compositions of pyrite (a) and pyrrhotite (b) in the ores from the
679 Wulong gold deposit.
680
681 Figure 7. Theoretical $^{56}Fe/^{54}Fe$ fractionation using equations (1) and (2). References for the
682 reduced partition functions are listed in the text. The reduced partition functions of Fe^{2+}_{aq}
683 (Rustad and Dixon, 2009), pyrite (Blanchard et al. 2009), chalcopyrite (Polyakov and Soultanov
684 2011), magnetite and pyrrhotite (Polyakov et al. 2007) were used. (a) Reduced partition function
685 ratios ($10^3 ln\beta^{56/54}Fe$) for pyrite, chalcopyrite, magnetite, pyrrhotite, and Fe^{2+}_{aq}. (b) Theoretical
686 iron isotopic fractionation between minerals and a Fe^{2+} bearing aqueous solution ($10^3 \ln$
687 $\alpha^{56}Fe_{mineral\text{-}fluid}$).
688
689 Figure 8. Model fractionation of Fe isotopes in a closed system for the pyrite- pyrrhotite -
690 solution system at 300°C. The same reduced partition functions as listed in Fig.7 were used. The
691 evolution lines of ore-forming fluids during pyrite and pyrrhotite precipitation were calculated
692 using the Rayleigh fractionation formula: $\delta^{56}Fe_{fluid}=F^{(\alpha\ mineral\text{-}fluid\ -1)}\times(\ \delta^{56}Fe_{fluid}{}^{0}+1000)-1000$,
693 where $\delta^{56}Fe_{fluid}{}^{0}$ is the initial Fe isotopic value and F is the fraction of Fe remaining in the fluid.
694 (a) Assuming that pyrite crystallized first, the calculated $\delta^{56}Fe$ values of the remaining fluids will
695 gradually decrease as precipitation of pyrite proceeds, and the $\delta^{56}Fe$ values of ore-forming fluids
696 would be higher than those of quartz separates. (b) The calculated $\delta^{56}Fe$ values of the remaining
697 fluids are inconsistent with quartz separates if pyrite and pyrrhotite co-crystallized. (c) Assuming
698 the pyrrhotite crystallized first, the $\delta^{56}Fe$ values of remaining fluids are consistent with those of
699 quartz separates.
700

Figure 9. Temperature (°C) vs. oxygen fugacity (logfO_2) diagram (after Wawryk and Foden 2017) showing the inferred evolution path for the Wulong deposit. The schematic evolution trajectory from porphyry Cu-Au deposits is from Li et al. (2018).
Mineral abbreviations: Py = pyrite, Po = pyrrhotite, Cpy = chalcopyrite, Bn = bornite, Mt = magnetite, Hm = hematite.

Figure 10. Comparison of Fe and S isotopes in Wulong sulfides and those from Jiaodong gold deposits (data from Zhu et al. 2018).

Figure 11. Iron isotope data from Wulong sulfides compared to other deposits. (a) Pyrite from porphyry deposit (Li et al., 2018), skarn deposits (Wang et al. 2011, 2015), porphyry-skarn deposit (Graham et al. 2004), hydrothermal W-Sn deposit (Wawryk and Foden 2015), and Jiaodong gold deposits (Zhu et al. 2018). (b) Pyrrhotite from magmatic Ni-Cu deposits (Bilenker et al. 2018; Ding et al. 2019), skarn deposit (Wang et al. 2015), hydrothermal W-Sn deposit (Wawryk and Foden 2015).

Table 1. Iron isotopic compositions from this study.

Sample number	Sample location	Sample type description	Mineral/Whole rock	δ^{56}Fe(‰)	2SD(‰)	δ^{57}Fe(‰)	2SD(‰)	n
WL18-66	-636m in No.163 vein	Disseminated pyrite in diorite	Pyrite	0.41	0.03	0.64	0.17	3
WL18-82	-636m in No.163 vein	Disseminated pyrite in diorite	Pyrite	0.38	0.02	0.59	0.07	3
WL18-56	-636m in No.163 vein	Fine quartz-pyrrhotite-pyrite vein	Pyrite	0.40	0.01	0.59	0.05	3
WL18-56 r[a]	-636m in No.163 vein	Fine quartz-pyrrhotite-pyrite vein	Pyrite	0.42	0.09	0.60	0.08	3
WL18-92	-756m in No.163 vein	Fine quartz-pyrrhotite-pyrite vein	Pyrite	0.35	0.02	0.55	0.26	3
WL18-93	-756m in No.163 vein	Fine quartz-pyrrhotite-pyrite vein	Pyrite	0.38	0.01	0.59	0.01	3
WL18-49	-516m in No.163 vein	Thick quartz-pyrite-pyrrhotite vein	Pyrite	0.63	0.06	0.93	0.07	3
WL18-49 r[a]	-516m in No.163 vein	Thick quartz-pyrite-pyrrhotite vein	Pyrite	0.64	0.08	0.99	0.04	3
WL18-50	-516m in No.163 vein	Thick quartz-pyrite-pyrrhotite vein	Pyrite	0.11	0.03	0.23	0.11	3
WL18-51	-516m in No.163 vein	Thick quartz-pyrite-pyrrhotite vein	Pyrite	0.39	0.05	0.56	0.05	3
WL18-52	-516m in No.163 vein	Thick quartz-pyrite-pyrrhotite vein	Pyrite	0.32	0.02	0.55	0.02	3

WL18-53	-516m in No.163 vein	Thick quartz-pyrite-pyrrhotite vein	Pyrite	0.78	0.03	1.24	0.00	3
WL18-56	-636m in No.163 vein	Fine quartz-pyrrhotite-pyrite vein	Pyrrhotite	-0.51	0.07	-0.69	0.04	3
WL18-56 r[a]	-636m in No.163 vein	Fine quartz-pyrrhotite-pyrite vein	Pyrrhotite	-0.48	0.09	-0.65	0.09	3
WL18-92	-756m in No.163 vein	Fine quartz-pyrrhotite-pyrite vein	Pyrrhotite	-0.55	0.01	-0.78	0.02	3
WL18-93	-756m in No.163 vein	Fine quartz-pyrrhotite-pyrite vein	Pyrrhotite	-0.54	0.06	-0.70	0.02	3
WL18-50	-516m in No.163 vein	Thick quartz-pyrite-pyrrhotite vein	Pyrrhotite	-0.72	0.07	-1.08	0.09	3
WL18-50 r[a]	-516m in No.163 vein	Thick quartz-pyrite-pyrrhotite vein	Pyrrhotite	-0.70	0.08	-1.03	0.02	3
WL18-52	-516m in No.163 vein	Thick quartz-pyrite-pyrrhotite vein	Pyrrhotite	-0.35	0.01	-0.46	0.02	3
WL18-53	-516m in No.163 vein	Thick quartz-pyrite-pyrrhotite vein	Pyrrhotite	-0.07	0.00	-0.13	0.04	3
WL18-90	-756m in No.163 vein	Thick quartz-pyrite-pyrrhotite vein	Pyrrhotite	-0.82	0.04	-1.14	0.07	3
WL18-91	-756m in No.163 vein	Thick quartz-pyrite-pyrrhotite vein	Pyrrhotite	-0.82	0.02	-1.21	0.02	3
WL18-85	-636m in No.163 vein	Thick quartz-pyrite-pyrrhotite vein	Pyrrhotite	-0.85	0.01	-1.25	0.13	3

WL18-86	-636m in No.163 vein	Thick quartz-pyrite-pyrrhotite vein	Pyrrhotite	-0.31	0.00	-0.38	0.02	3
WL18-85	-636m in No.163 vein	Thick quartz-pyrite-pyrrhotite vein	Quartz	-0.02	0.02	0.00	0.06	3
WL18-86	-636m in No.163 vein	Thick quartz-pyrite-pyrrhotite vein	Quartz	0.07	0.07	0.11	0.10	3
AGV-2		Andesite standard	Whole rock	0.12	0.03	0.19	0.09	9
G-2		Granite standard	Whole rock	0.15	0.05	0.23	0.05	9
GSP-2		Granodiorite standard	Whole rock	0.15	0.05	0.21	0.09	6

Note r[a] in sample name denotes a replicate digestion and analysis of the same sample.

Table 2. In situ S isotopic compositions of pyrite and pyrrhotite in the Wulong gold deposit.

Sample	Mineral	$\delta^{34}S$(‰)	Sample	Mineral	$\delta^{34}S$(‰)
WL12-4-PO-1	pyrrhotite	0.7	WL12-4-PY-1	pyrite	1.9
WL12-4-PO-2	pyrrhotite	0.2	WL12-4-PY-2	pyrite	1.8
WL18-86-PO-1	pyrrhotite	-0.2	WL18-66-PY-1	pyrite	2.5
WL18-86-PO-2	pyrrhotite	-0.5	WL18-66-PY-2	pyrite	3.0
WL18-56-PO-1	pyrrhotite	0.5	WL18-90-PY-1	pyrite	3.0
WL18-56-PO-2	pyrrhotite	0.0	WL18-90-PY-2	pyrite	2.9
WL18-92-PO-3	pyrrhotite	-1.2	WL18-49-PY-1	pyrite	0.5
WL18-92-PO-2	pyrrhotite	1.2	WL18-49-PY-2	pyrite	3.0
WL18-93-PO-1	pyrrhotite	0.7	WL18-51-PY-1	pyrite	2.9
WL18-93-PO-2	pyrrhotite	-0.3	WL18-51-PY-2	pyrite	3.0
WL18-92-PO-1	pyrrhotite	0.2	WL18-56-PY-1	pyrite	1.7
WL18-66-PO-1	pyrrhotite	0.3	WL18-56-PY-2	pyrite	1.9
WL18-66-PO-2	pyrrhotite	0.0	WL18-92-PY-1	pyrite	2.0
WL18-90-PO-1	pyrrhotite	0.2	WL18-92-PY-2	pyrite	2.0
WL18-90-PO-2	pyrrhotite	0.3	WL18-93-PY-1	pyrite	2.0
WL18-85-PO-1	pyrrhotite	-0.6	WL18-93-PY-2	pyrite	1.6
WL18-85-PO-2	pyrrhotite	0.7	WL18-50-PY-1	pyrite	2.2
WL18-50-PO-1	pyrrhotite	-0.1	WL18-50-PY-2	pyrite	2.1
WL18-50-PO-2	pyrrhotite	0.6	WL18-52-PY-1	pyrite	3.7
WL18-52-PO-1	pyrrhotite	0.8	WL18-52-PY-2	pyrite	4.1
WL18-52-PO-2	pyrrhotite	0.8	WL18-53-PY-1	pyrite	1.9
WL18-53-PO-1	pyrrhotite	0.0	WL18-53-PY-2	pyrite	1.9
WL18-53-PO-2	pyrrhotite	-0.1			

Figure 1

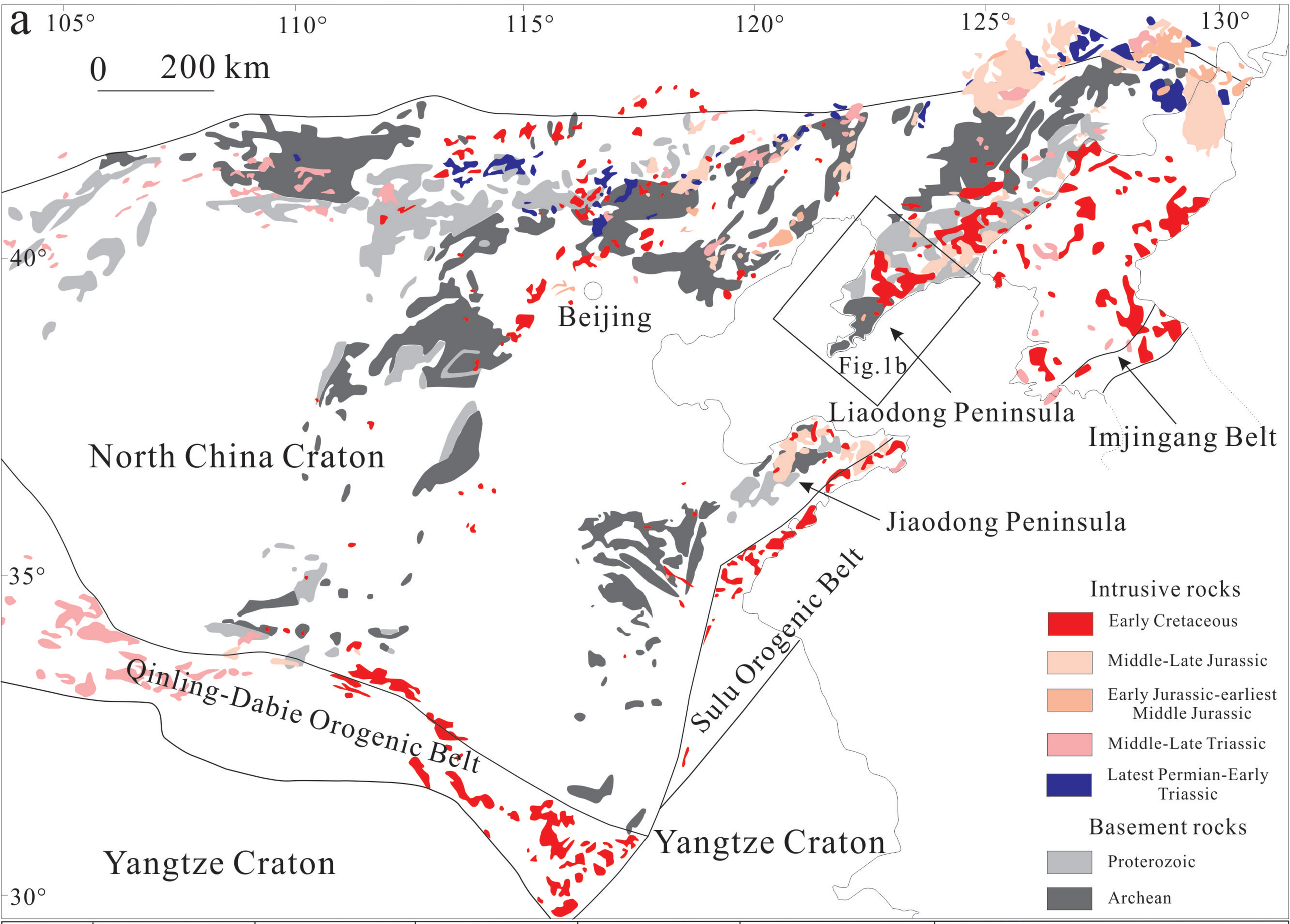
a
105°
110°
115°
120°
125°
130°
0 200 km
40°
35°
30°
Beijing
North China Craton
Fig.1b
Liaodong Peninsula
Imjingang Belt
Jiaodong Peninsula
Sulu Orogenic Belt
Qinling-Dabie Orogenic Belt
Yangtze Craton
Yangtze Craton
Intrusive rocks
Early Cretaceous
Middle-Late Jurassic
Early Jurassic-earliest Middle Jurassic
Middle-Late Triassic
Latest Permian-Early Triassic
Basement rocks
Proterozoic
Archean

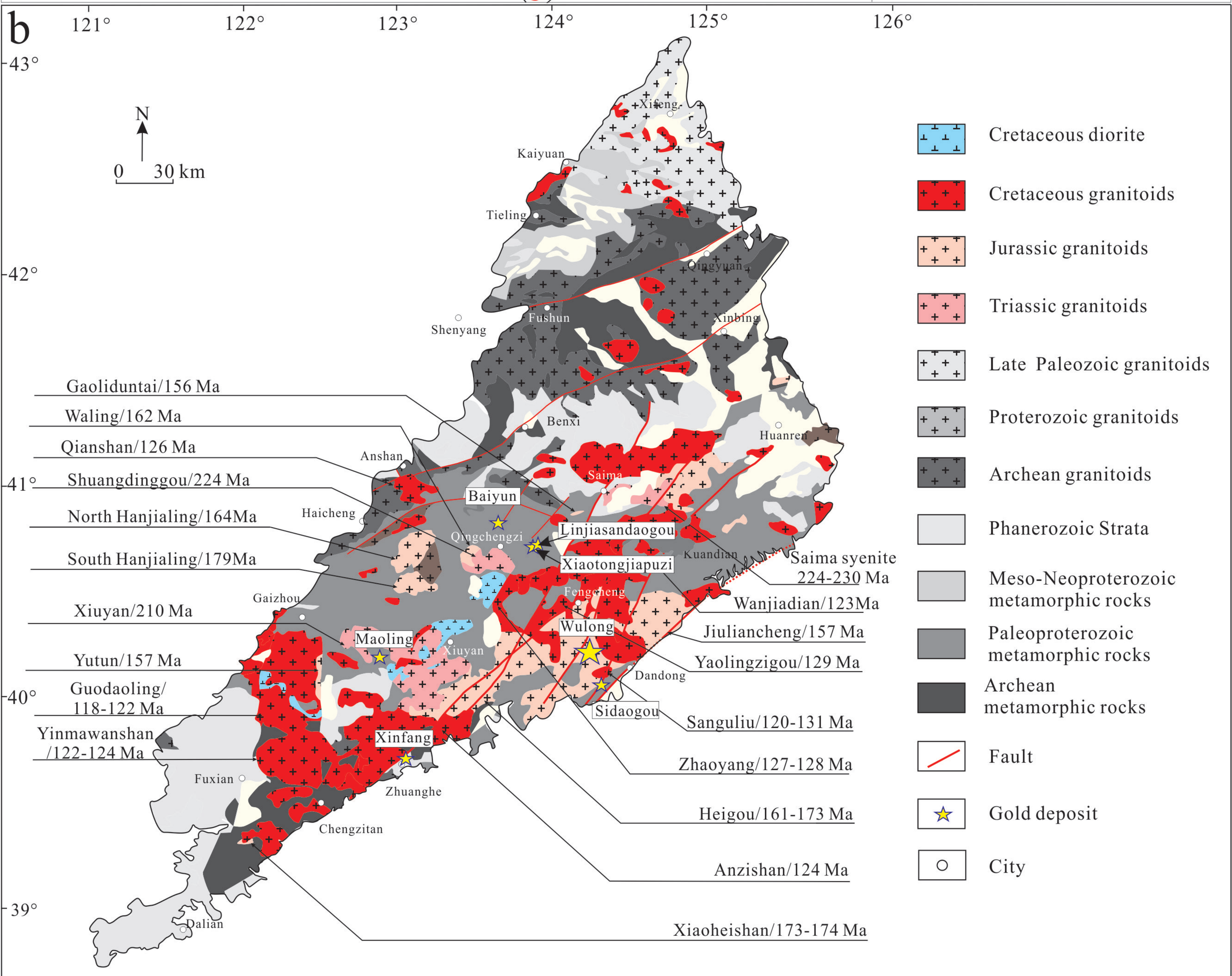
b
121°
122°
123°
124°
125°
126°
43°
42°
41°
40°
39°
N
0 30 km
Xifeng
Kaiyuan
Tieling
Qingyuan
Fushun
Shenyang
Xinbing
Benxi
Huanren
Anshan
Saima
Baiyun
Haicheng
Qingchengzi
Linjiasandaogou
Xiaotongjiapuzi
Kuandian
Saima syenite 224-230 Ma
Fengcheng
Gaizhou
Wanjiadian/123Ma
Wulong
Jiuliancheng/157 Ma
Maoling
Xiuyan
Yaolingzigou/129 Ma
Dandong
Sidaogou
Sanguliu/120-131 Ma
Xinfang
Zhaoyang/127-128 Ma
Fuxian
Zhuanghe
Heigou/161-173 Ma
Chengzitan
Anzishan/124 Ma
Dalian
Xiaoheishan/173-174 Ma
Gaoliduntai/156 Ma
Waling/162 Ma
Qianshan/126 Ma
Shuangdinggou/224 Ma
North Hanjialing/164Ma
South Hanjialing/179Ma
Xiuyan/210 Ma
Yutun/157 Ma
Guodaoling/ 118-122 Ma
Yinmawanshan /122-124 Ma
Cretaceous diorite
Cretaceous granitoids
Jurassic granitoids
Triassic granitoids
Late Paleozoic granitoids
Proterozoic granitoids
Archean granitoids
Phanerozoic Strata
Meso-Neoproterozoic metamorphic rocks
Paleoproterozoic metamorphic rocks
Archean metamorphic rocks
Fault
Gold deposit
City

Figure 2

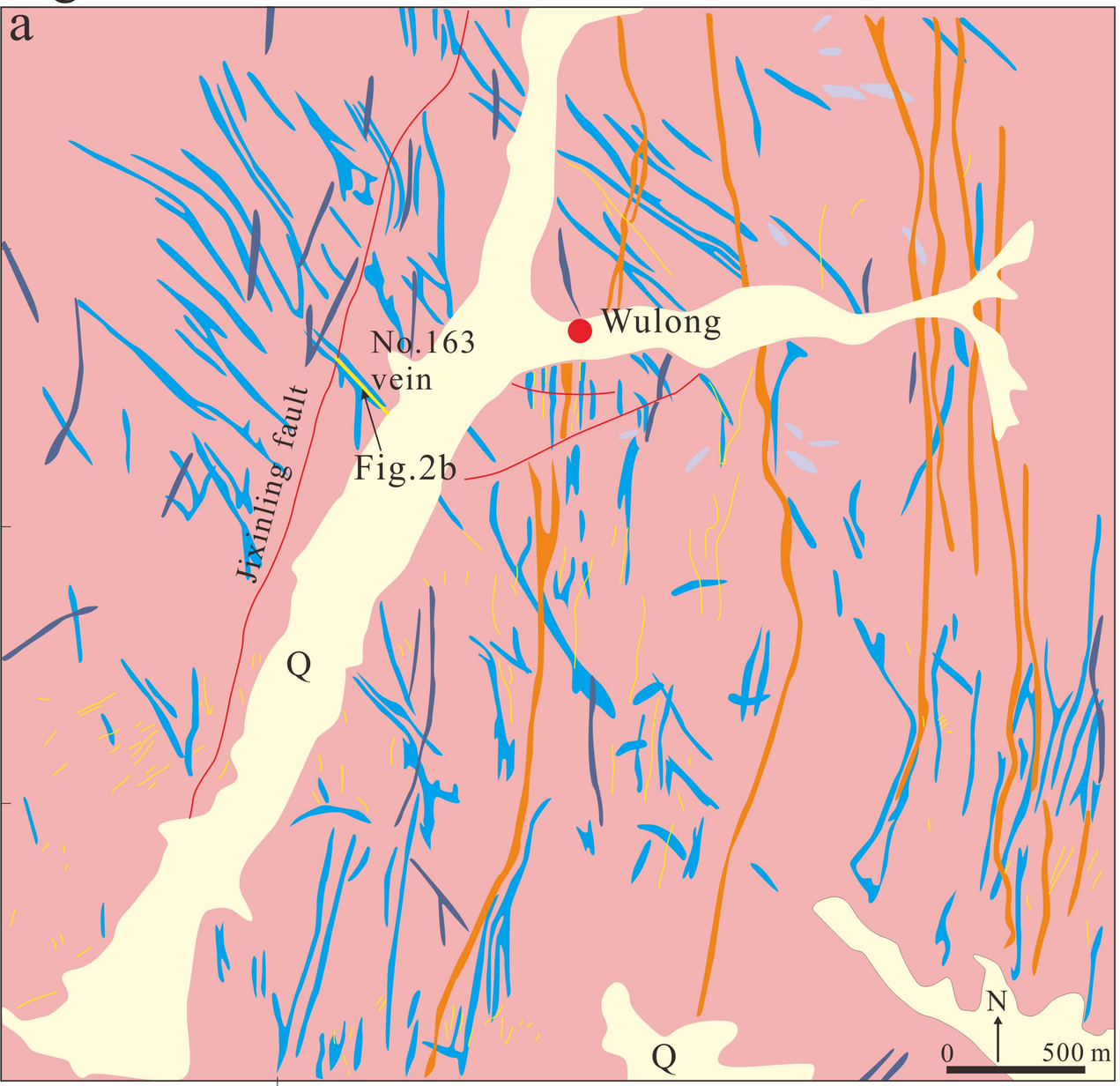
a
Wulong
No.163
vein
Fig.2b
Jixinling fault
Q
Q
N
0
500 m

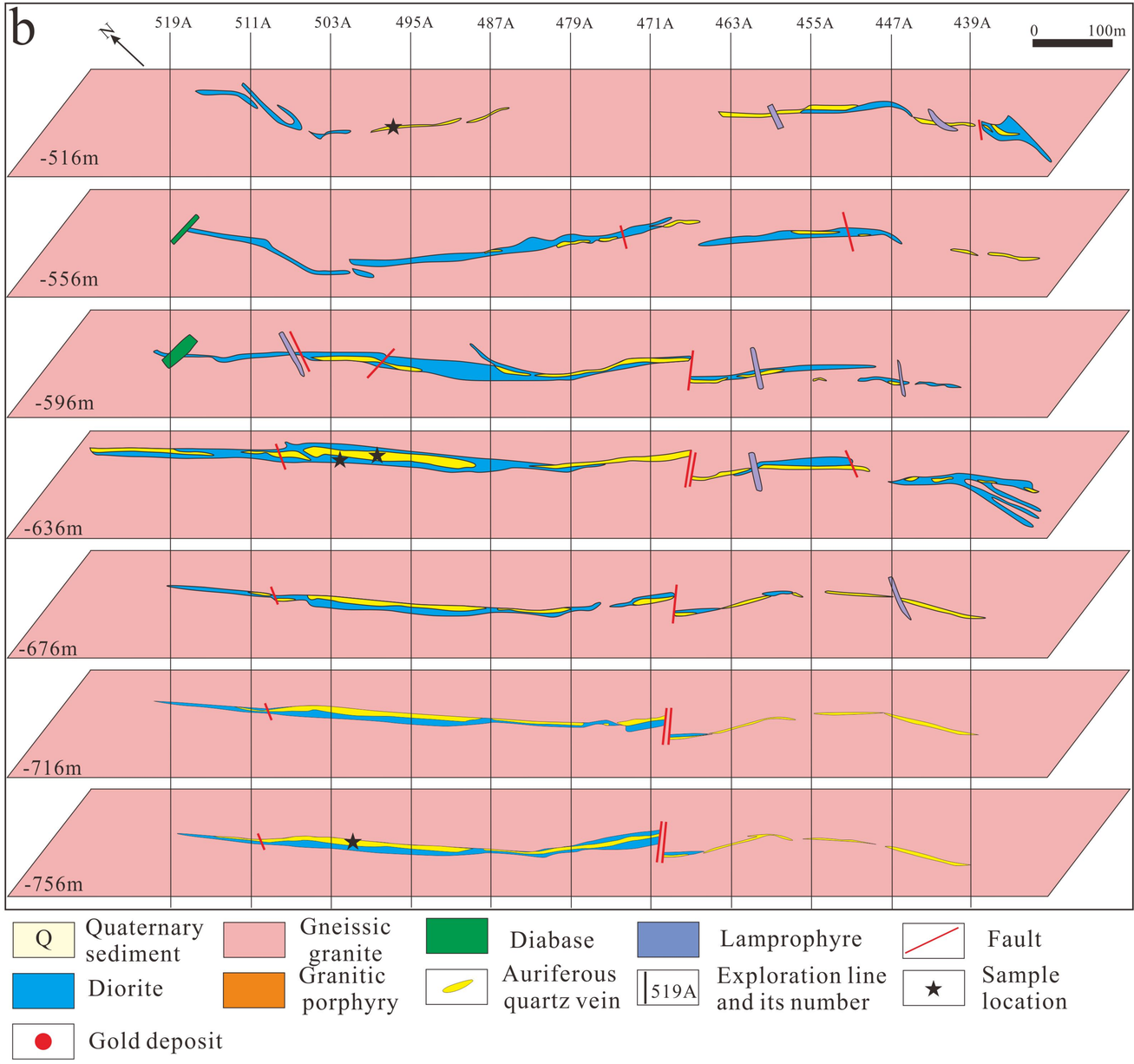
b
519A
511A
503A
495A
487A
479A
471A
463A
455A
447A
439A
0
100m
-516m
-556m
-596m
-636m
-676m
-716m
-756m
Q
Quaternary sediment
Diorite
Gold deposit
Gneissic granite
Granitic porphyry
Diabase
Auriferous quartz vein
Lamprophyre
519A
Exploration line and its number
Fault
Sample location

Figure 3

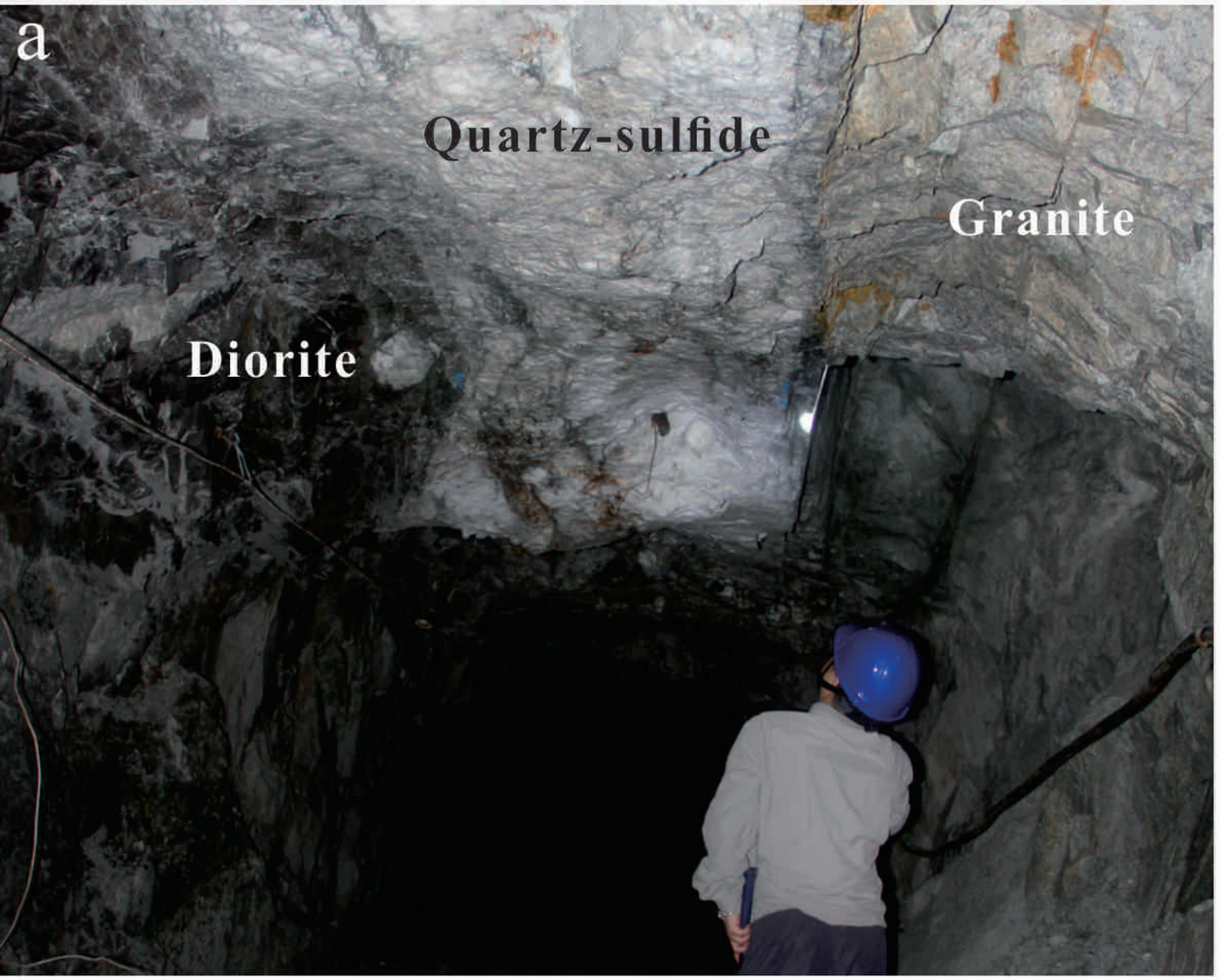
a
Quartz-sulfide
Granite
Diorite

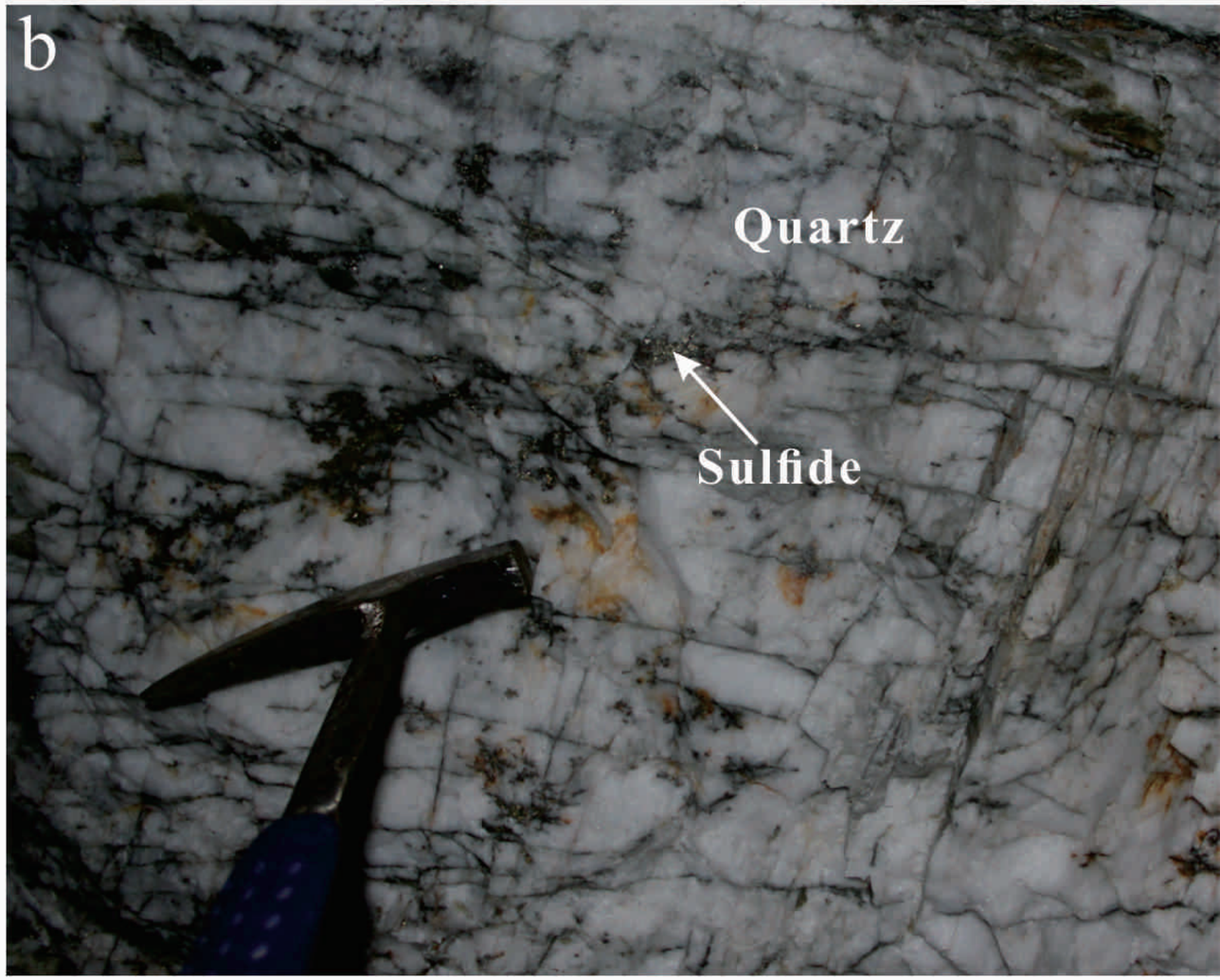
b
Quartz
Sulfide

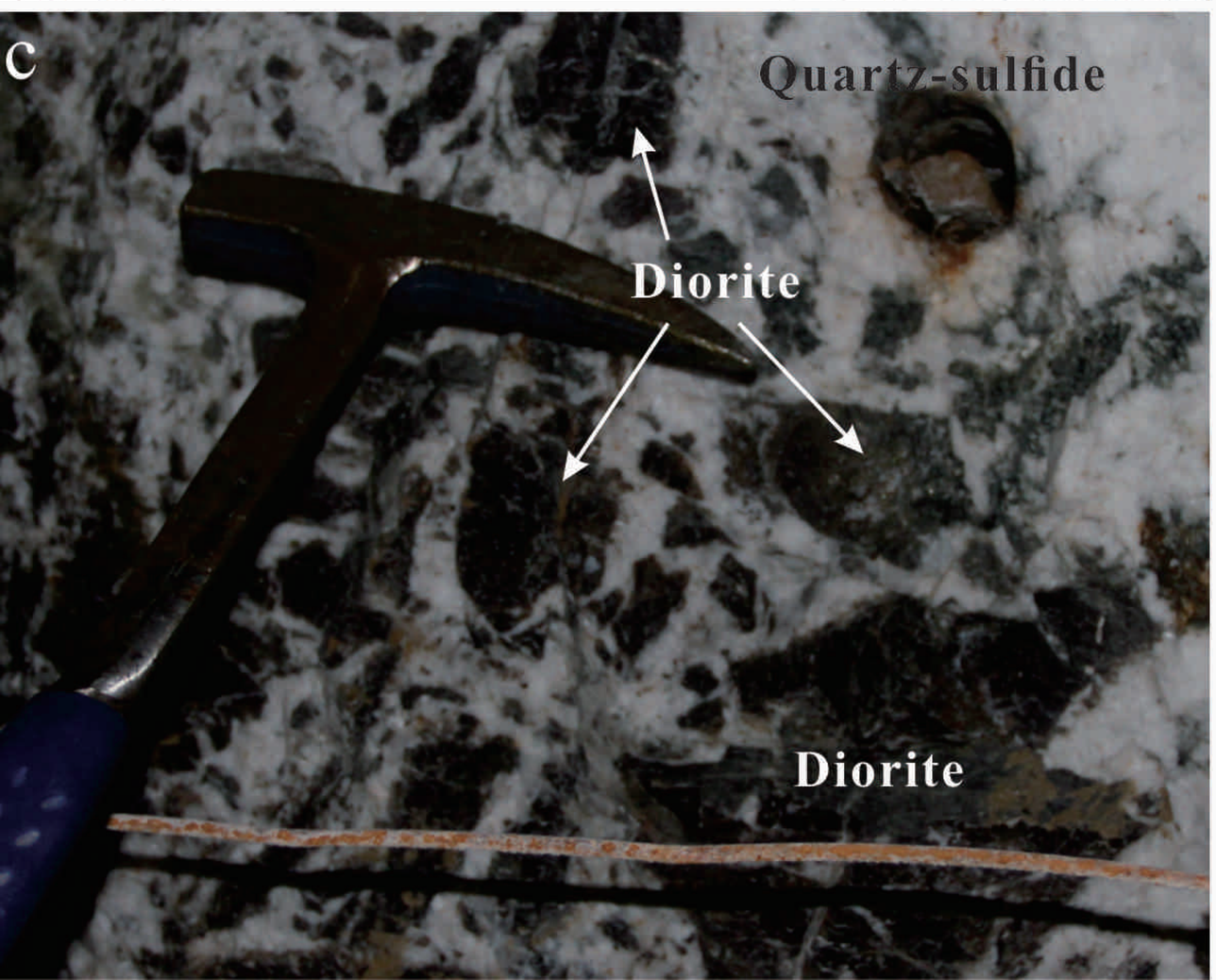
c
Quartz-sulfide
Diorite
Diorite

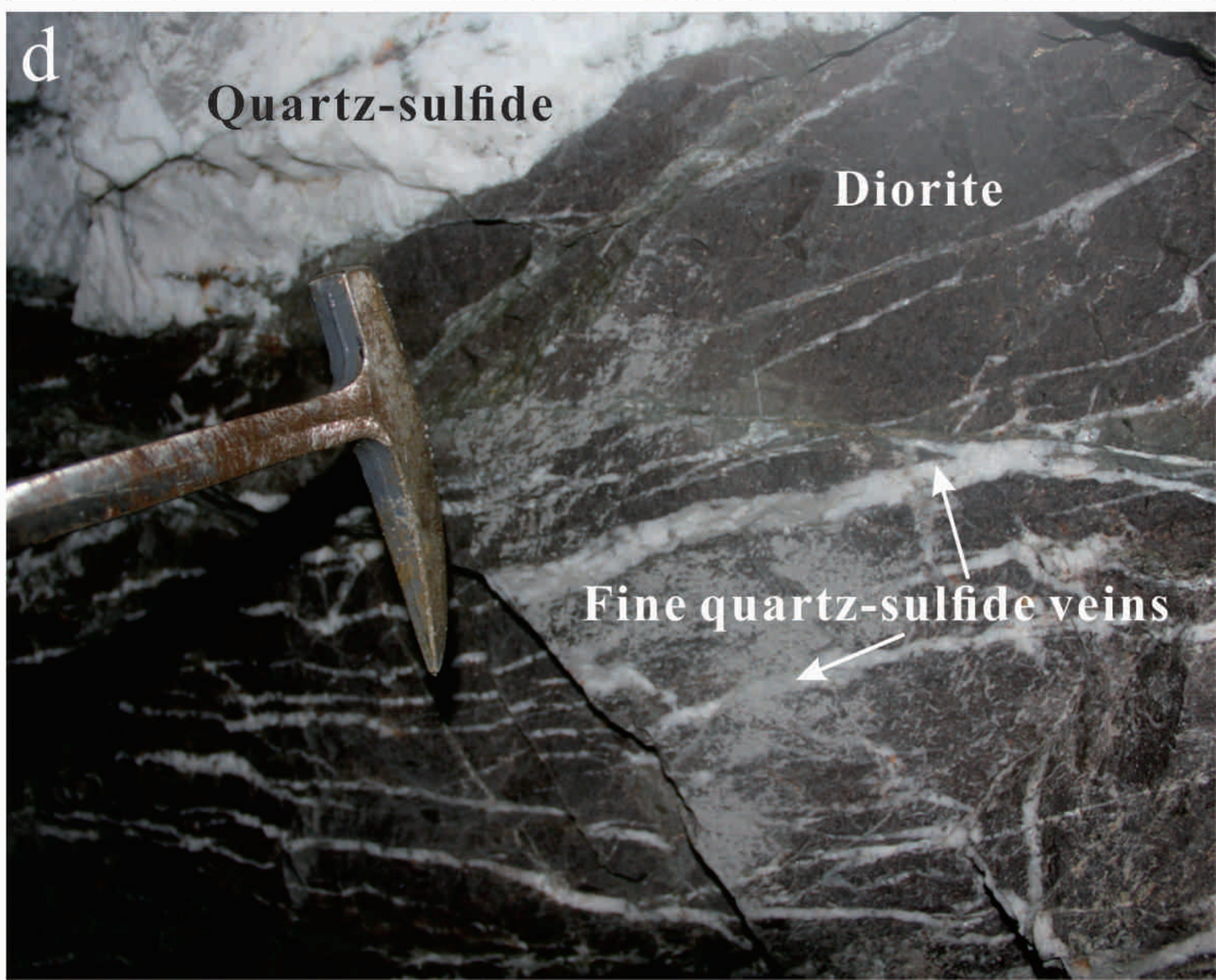
d
Quartz-sulfide
Diorite
Fine quartz-sulfide veins

Figure 4

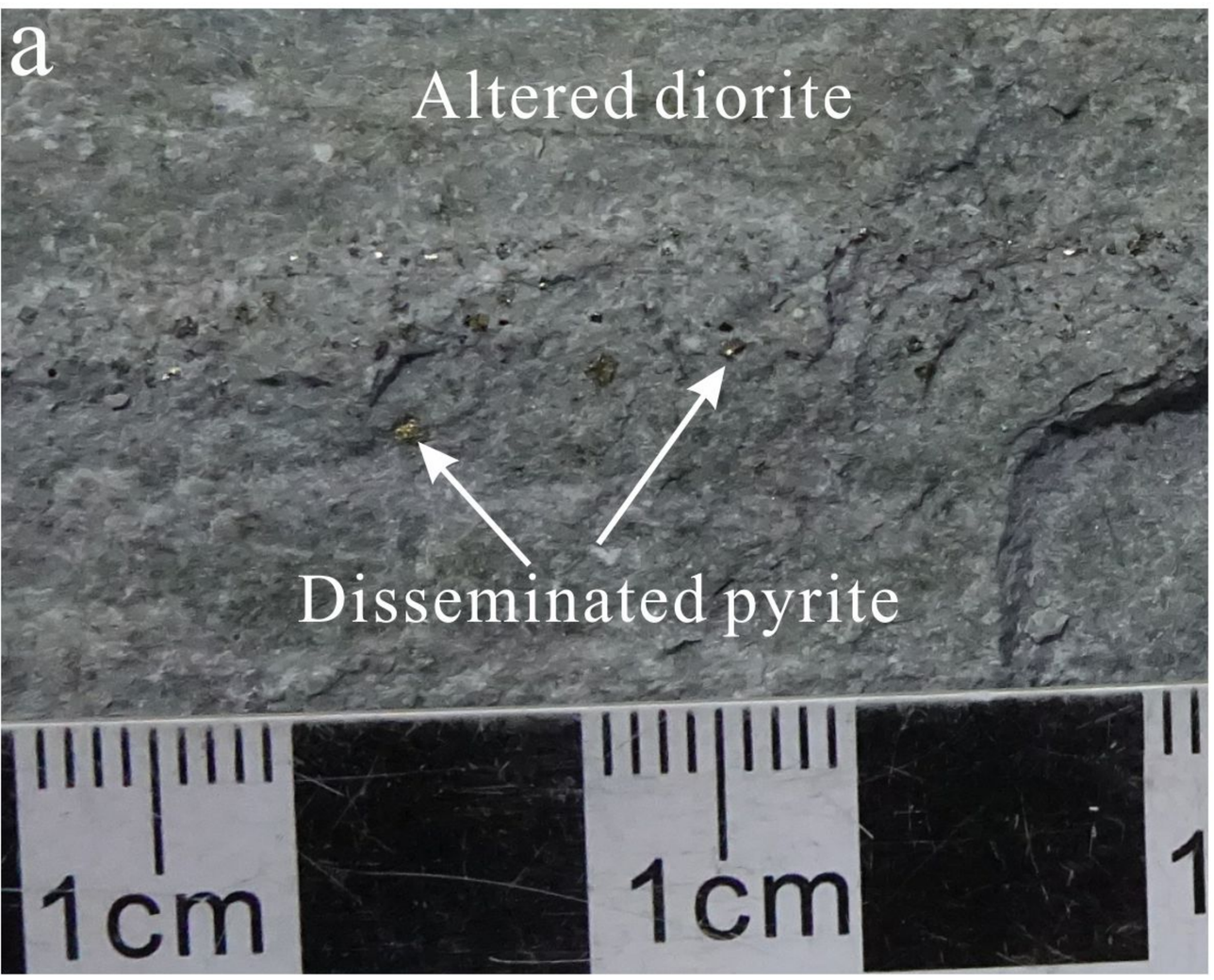
a
Altered diorite
Disseminated pyrite
1cm
1cm

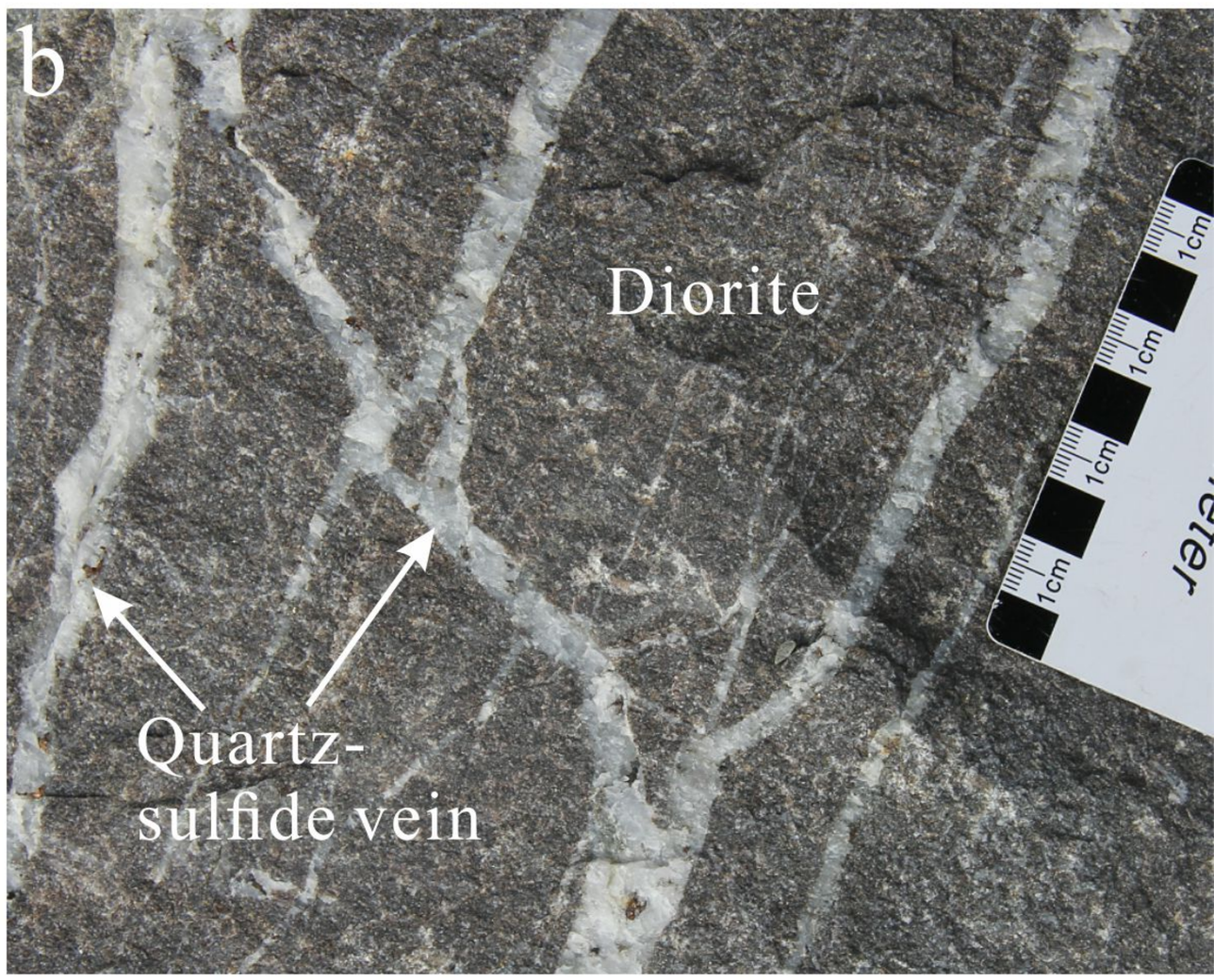
b
Diorite
Quartz-
sulfide vein
1cm
1cm
1cm

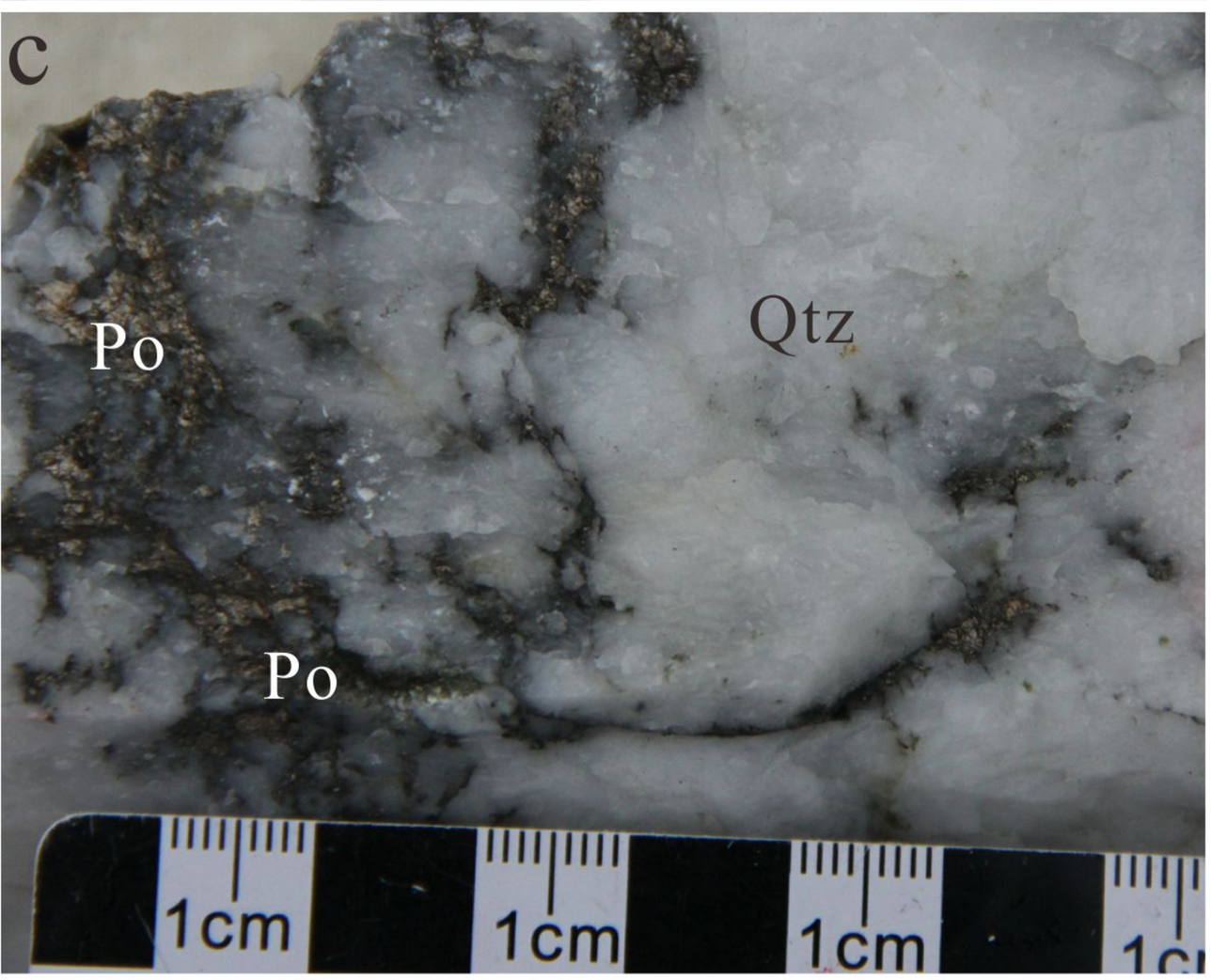
c
Po
Qtz
Po
1cm
1cm
1cm

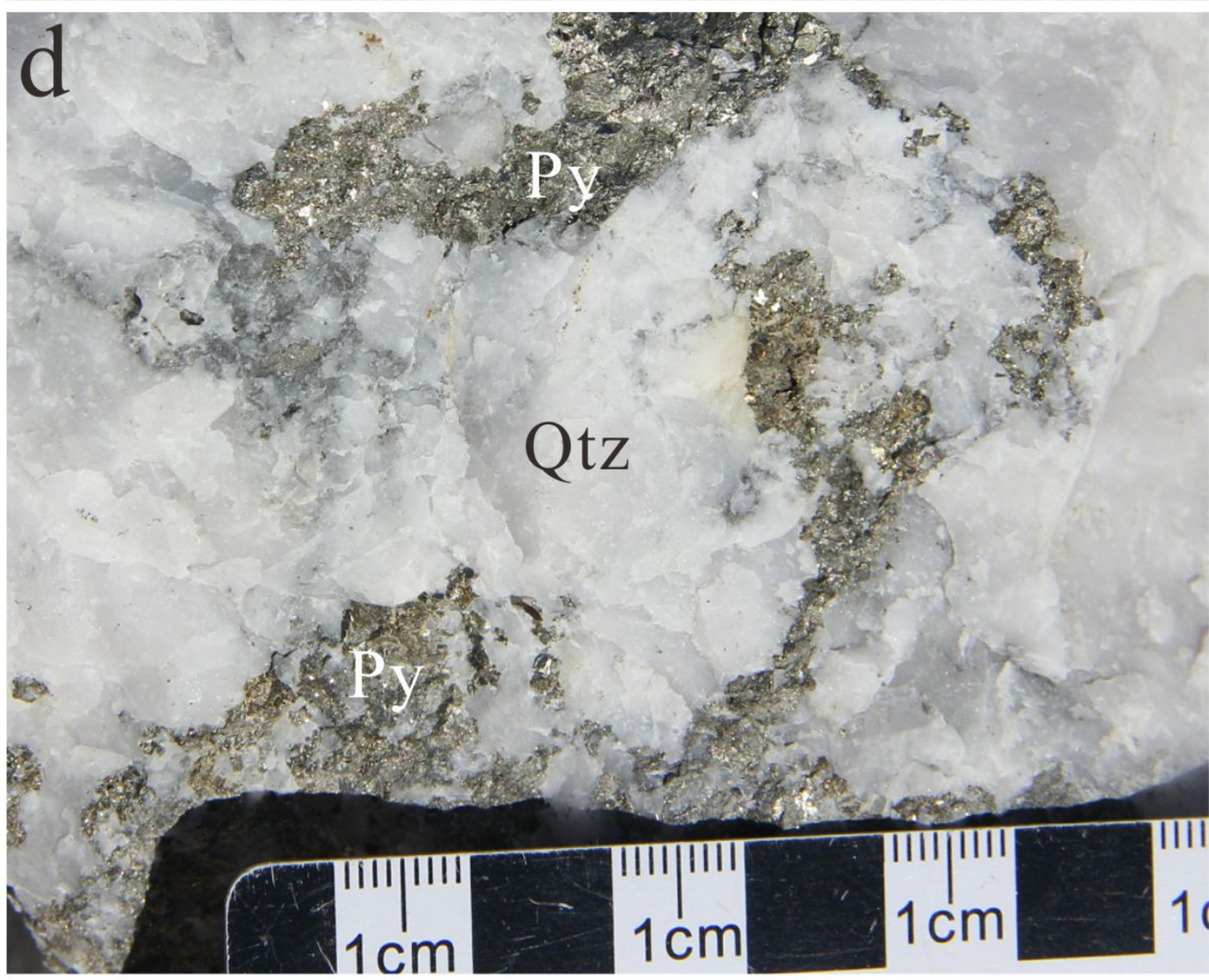
d
Py
Qtz
Py
1cm
1cm
1cm

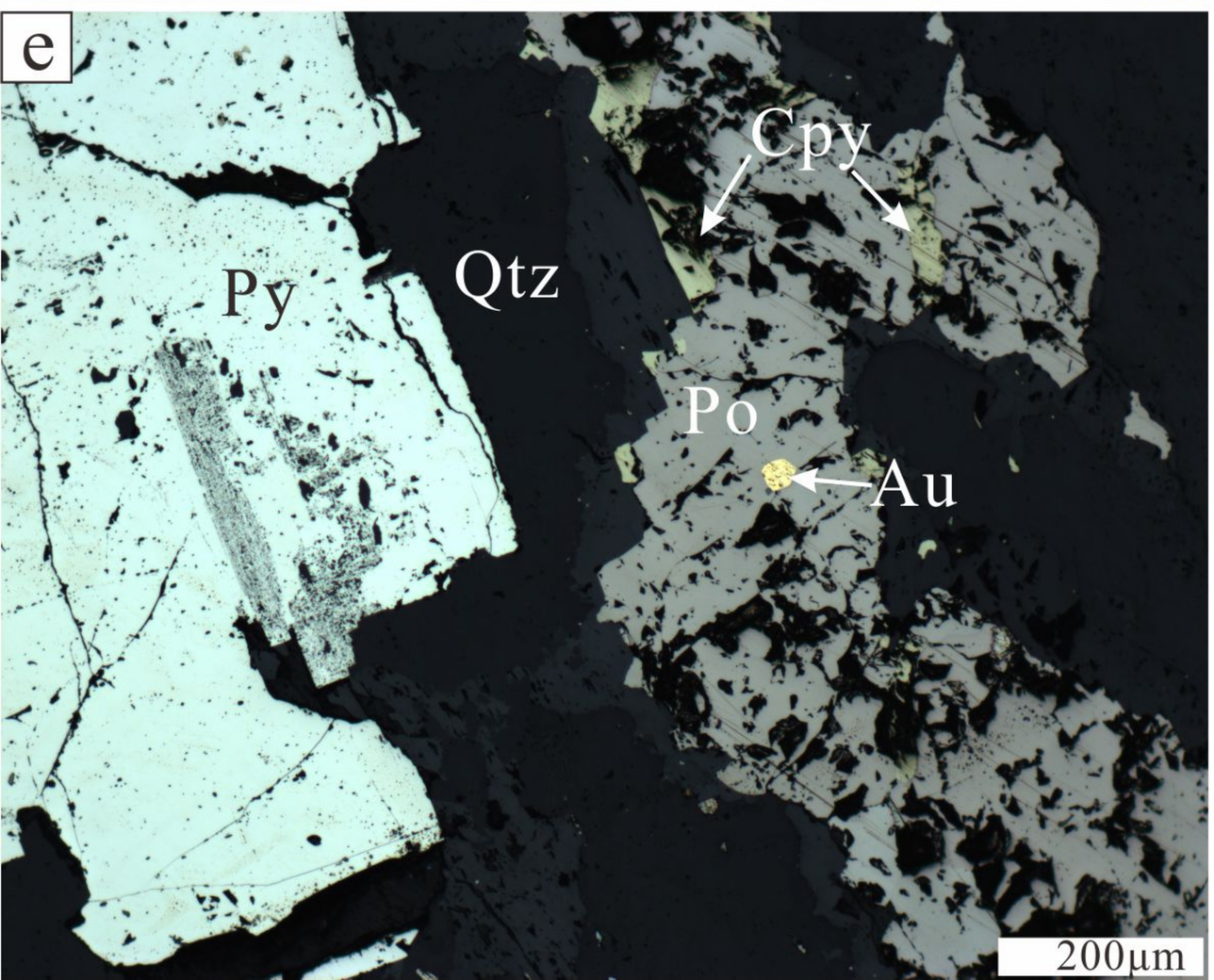
e
Py
Qtz
Cpy
Po
Au
200μm

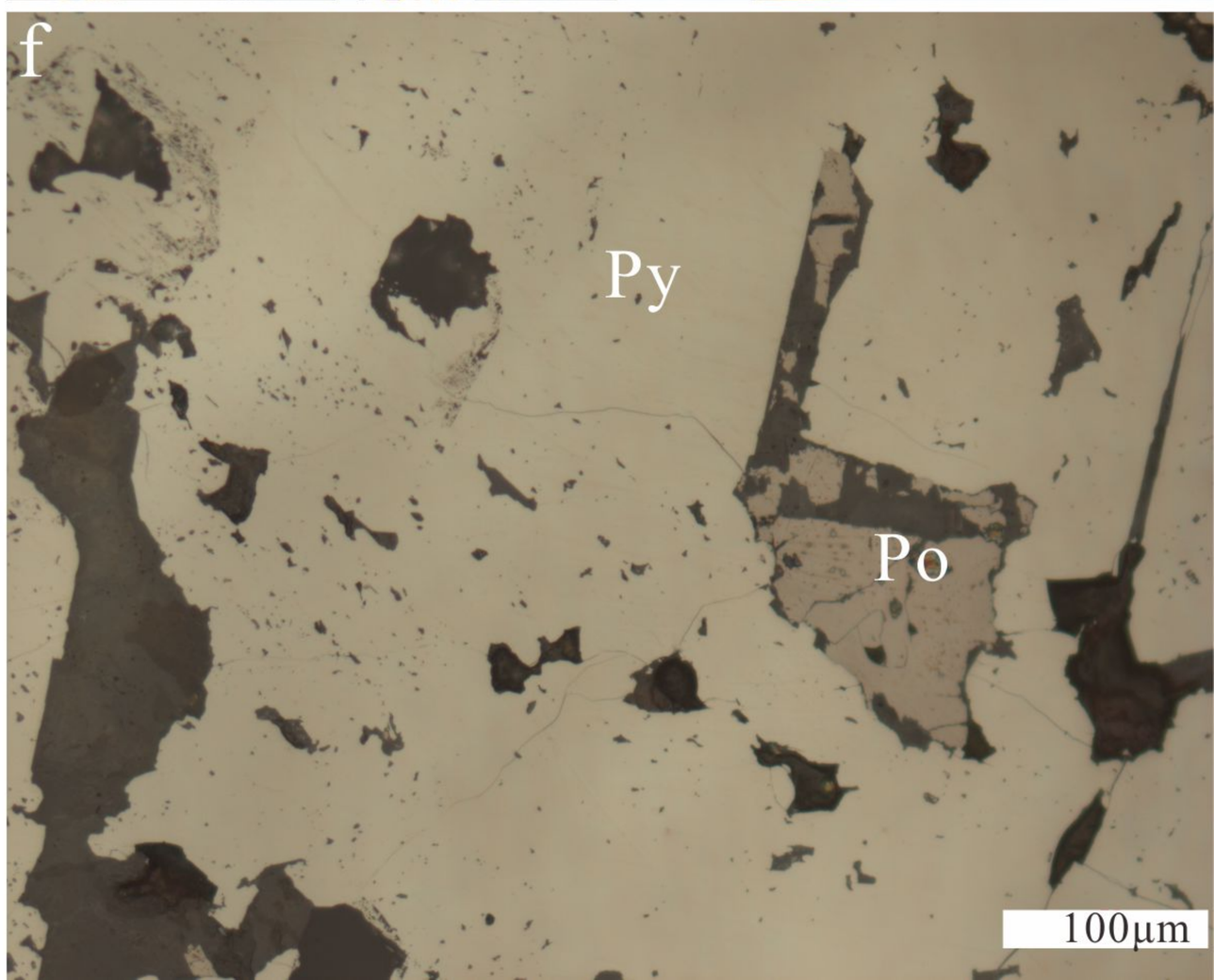
f
Py
Po
100μm

Figure 5

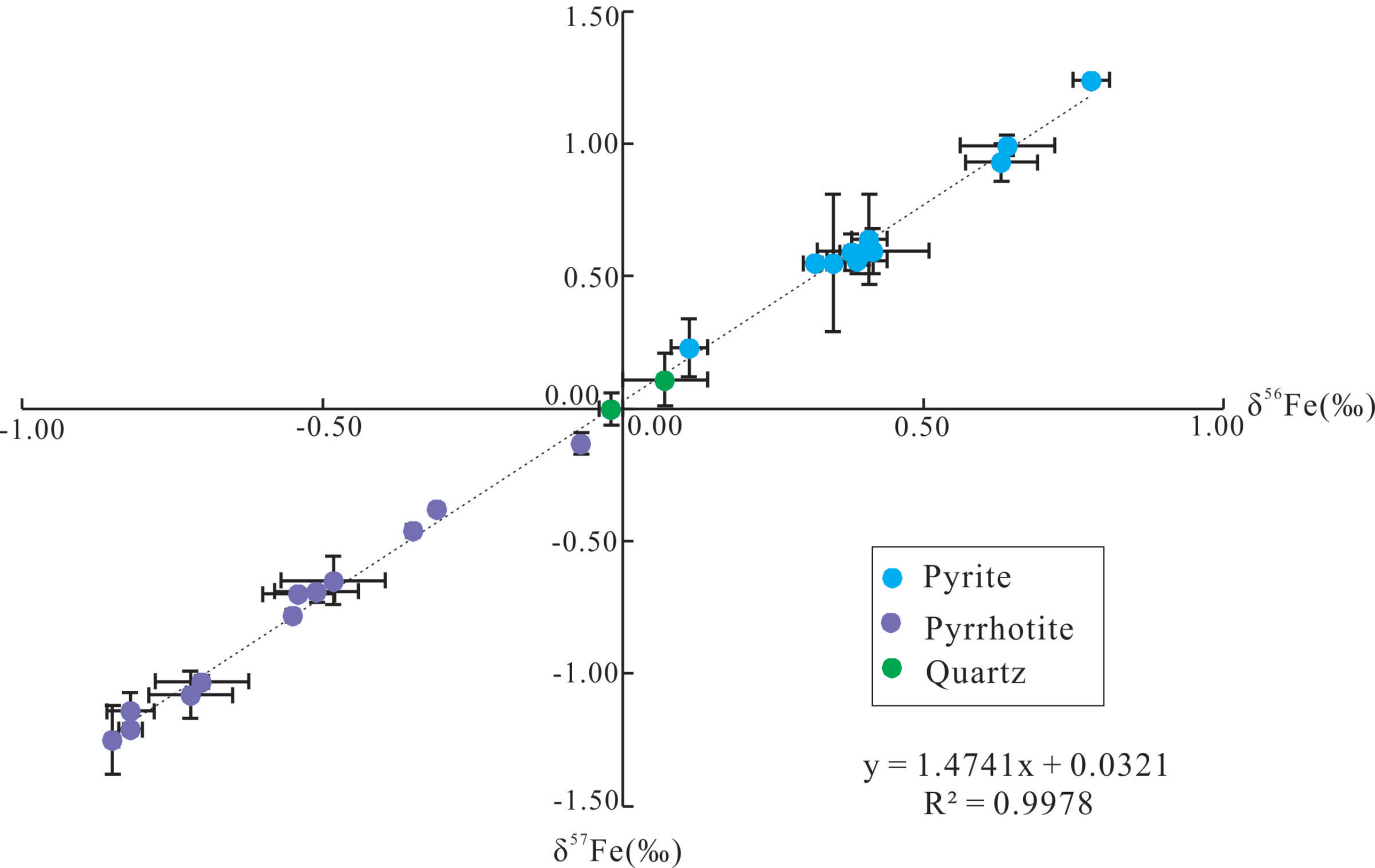
1.50
1.00
0.50
0.00
-0.50
-1.00
-1.50
-1.00
-0.50
0.00
0.50
1.00
δ56Fe(‰)
δ57Fe(‰)
Pyrite
Pyrrhotite
Quartz
y = 1.4741x + 0.0321
R² = 0.9978

Figure 6

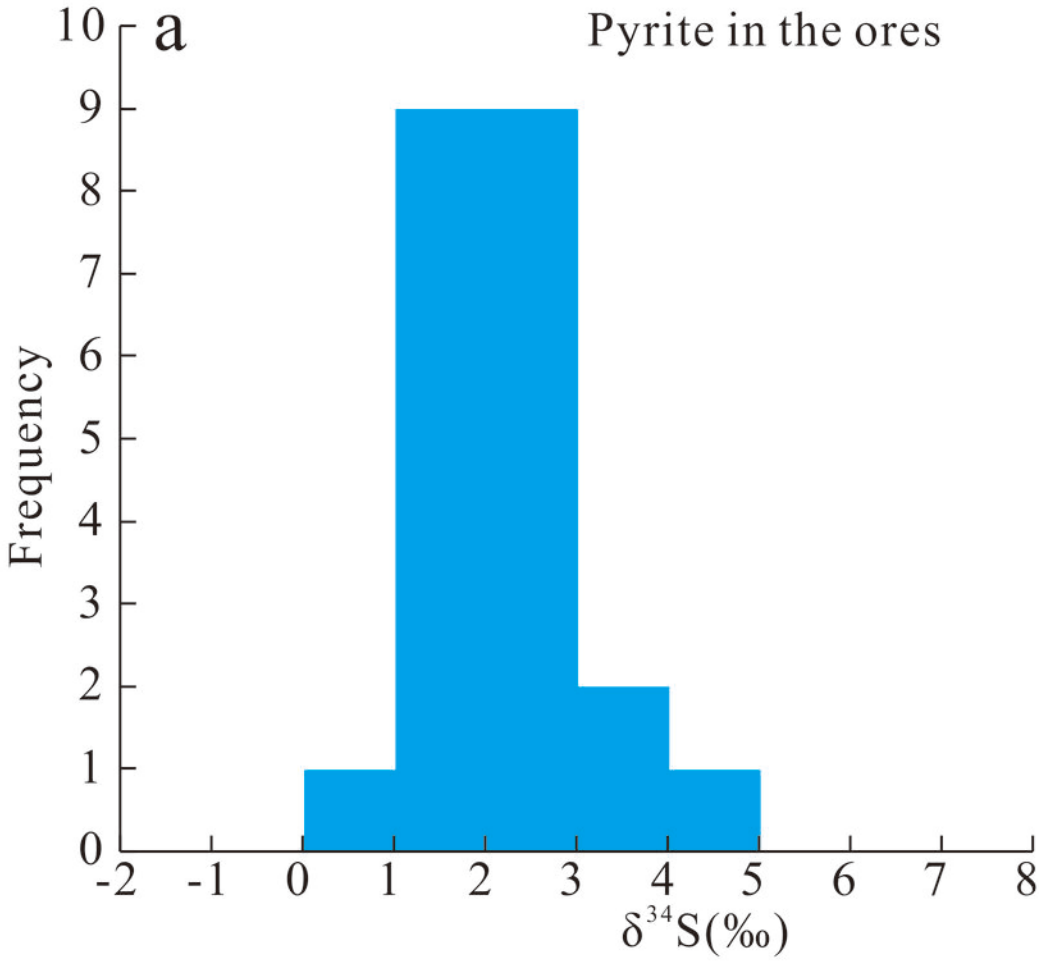
a
Pyrite in the ores
Frequency
10
9
8
7
6
5
4
3
2
1
0
-2
-1
0
1
2
3
4
5
6
7
8
δ34S(‰)

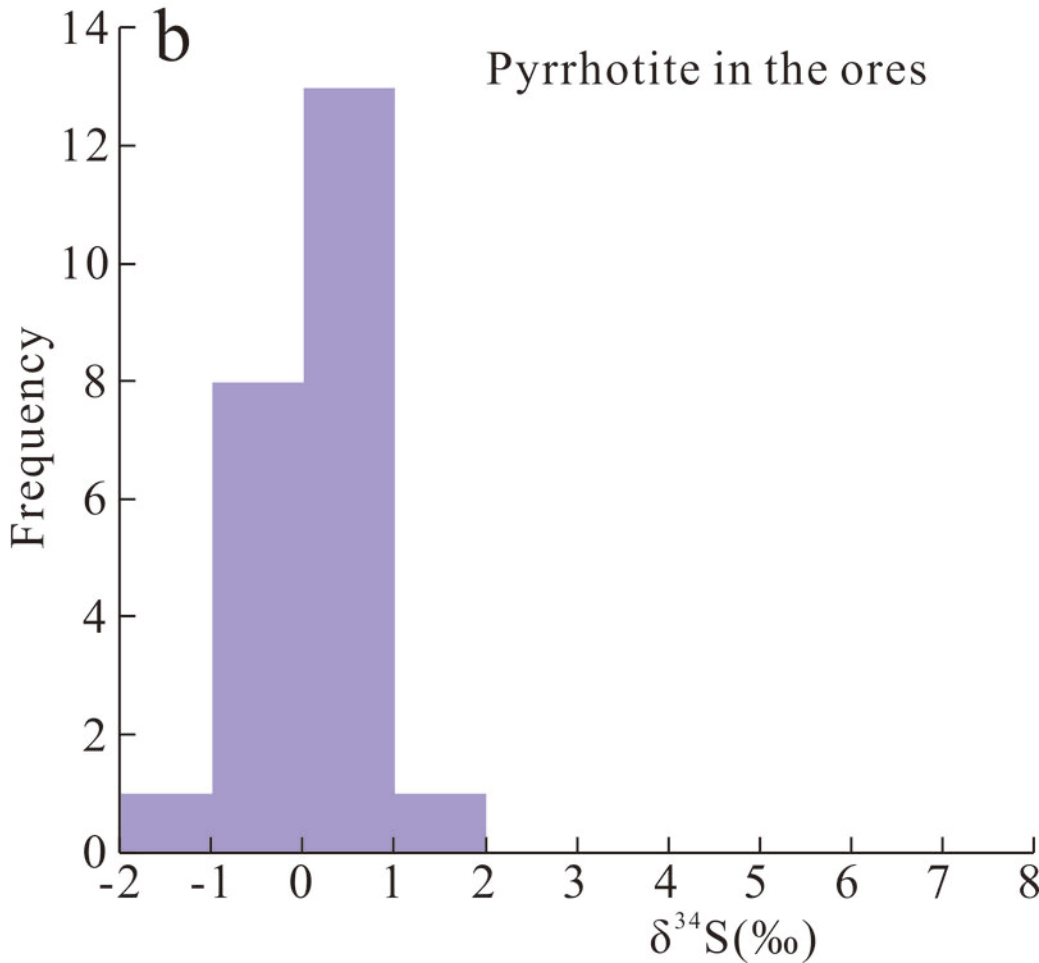
b
Pyrrhotite in the ores
Frequency
14
12
10
8
6
4
2
0
-2
-1
0
1
2
3
4
5
6
7
8
δ34S(‰)

Figure 7

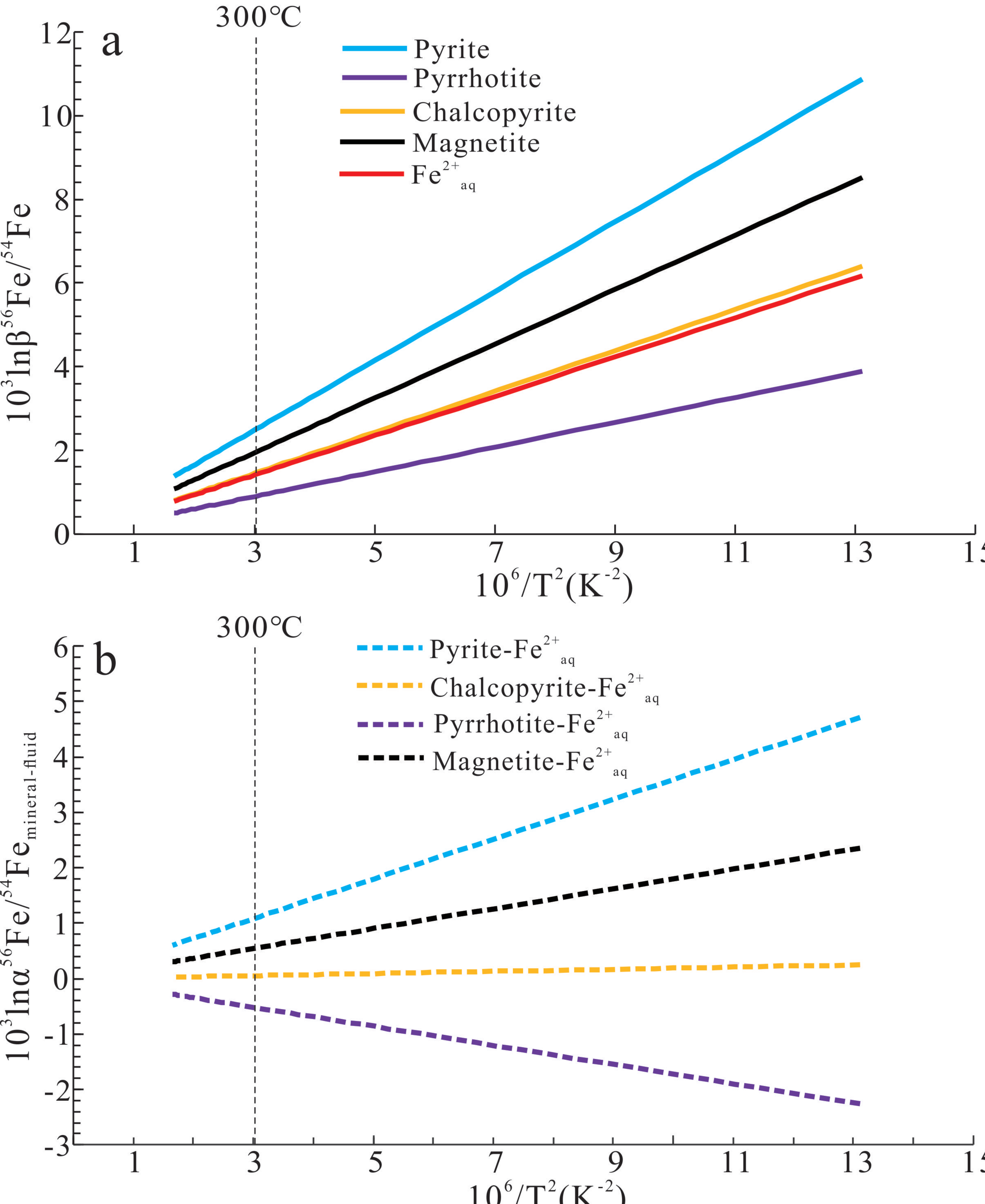
a
300℃
Pyrite
Pyrrhotite
Chalcopyrite
Magnetite
Fe^{2+}_{aq}
$10^3 ln\beta^{56}Fe/^{54}Fe$
$10^6/T^2(K^{-2})$
b
300℃
Pyrite-Fe^{2+}_{aq}
Chalcopyrite-Fe^{2+}_{aq}
Pyrrhotite-Fe^{2+}_{aq}
Magnetite-Fe^{2+}_{aq}
$10^3 ln\alpha^{56}Fe/^{54}Fe_{mineral\text{-}fluid}$
$10^6/T^2(K^{-2})$

Figure 8

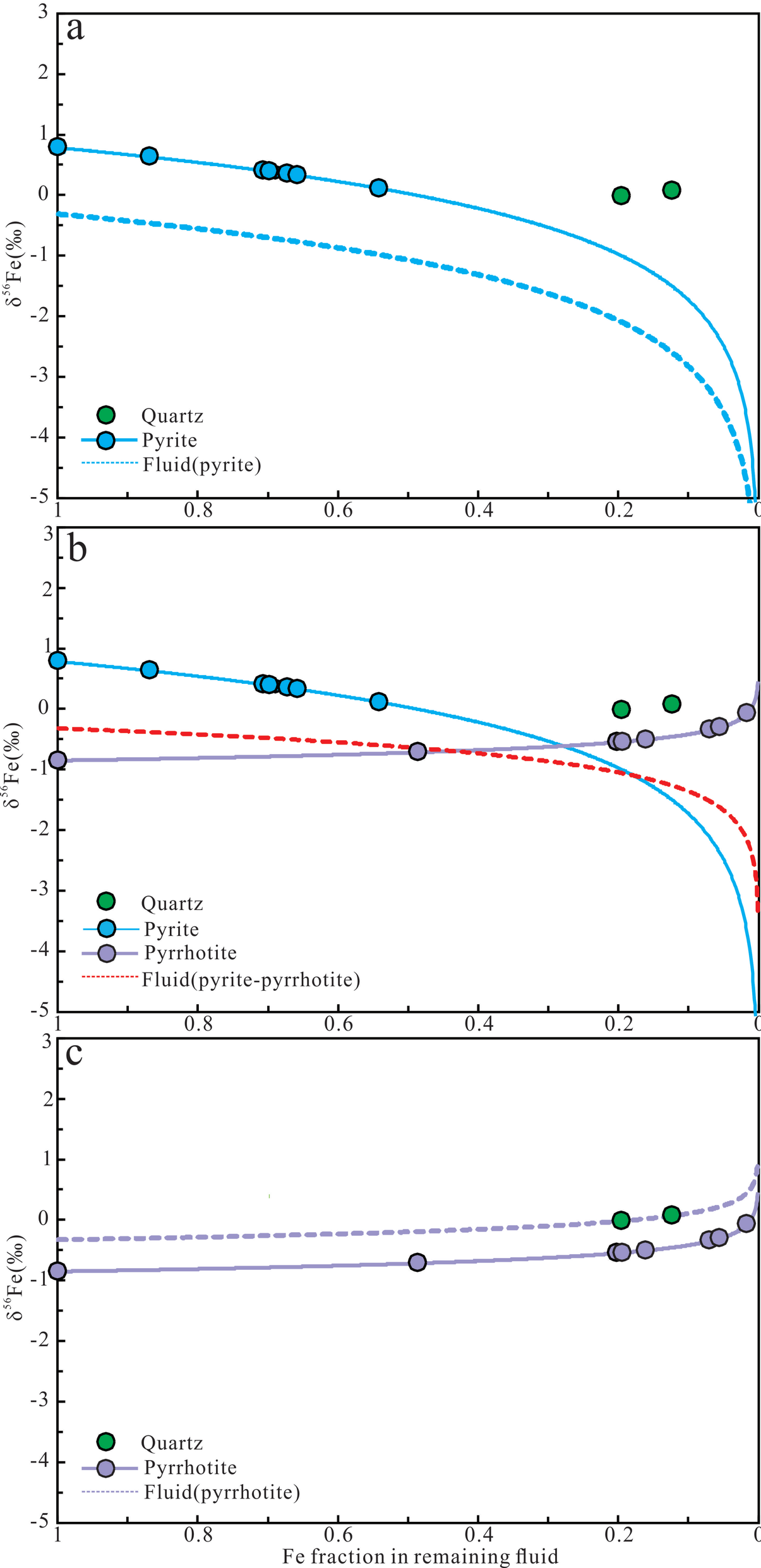
a
b
c
δ56Fe(‰)
Quartz
Pyrite
Fluid(pyrite)
Pyrrhotite
Fluid(pyrite-pyrrhotite)
Fluid(pyrrhotite)
Fe fraction in remaining fluid

Figure 9

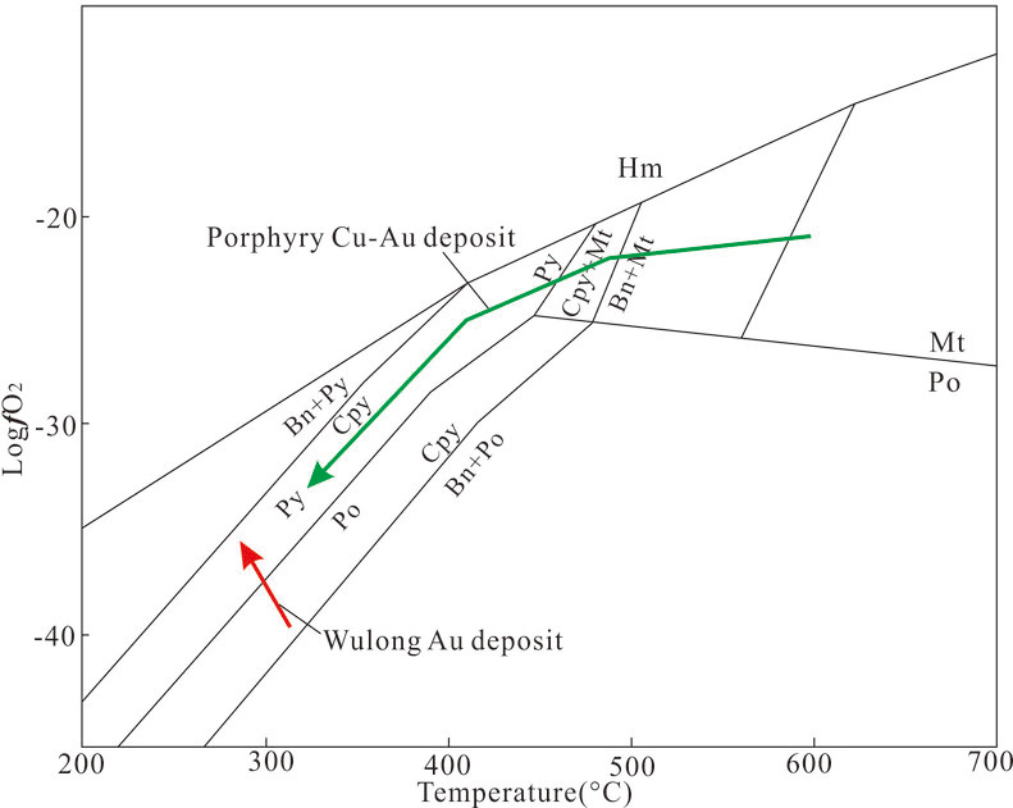
Hm
Porphyry Cu-Au deposit
Py
Cpy+Mt
Bn+Mt
Mt
Po
Bn+Py
Cpy
Py
Po
Cpy
Bn+Po
Wulong Au deposit
-20
-30
-40
LogfO2
200
300
400
500
600
700
Temperature(°C)

Figure 10

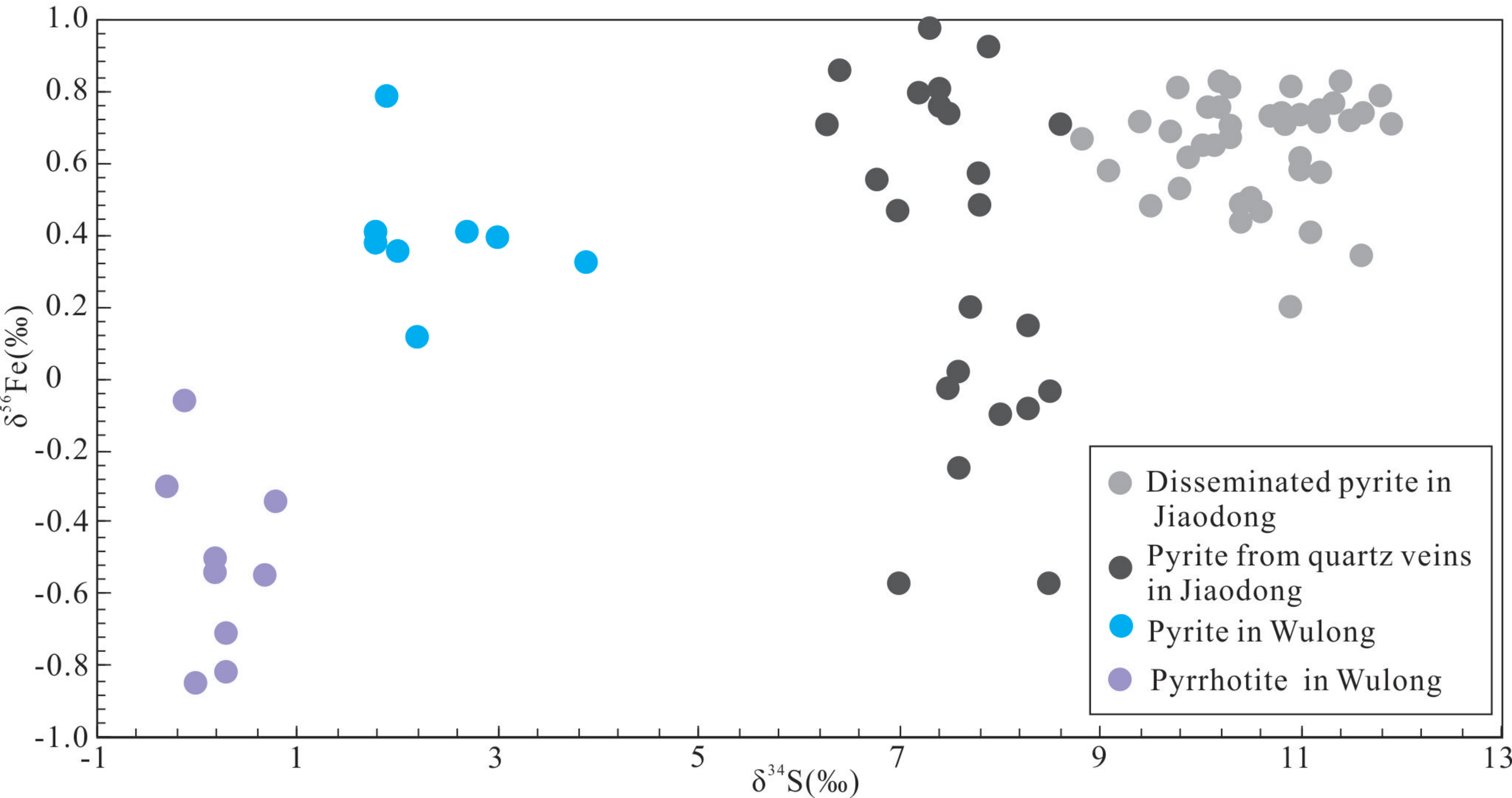
1.0
0.8
0.6
0.4
0.2
0
-0.2
-0.4
-0.6
-0.8
-1.0
δ56Fe(‰)
-1
1
3
5
7
9
11
13
δ34S(‰)
Disseminated pyrite in Jiaodong
Pyrite from quartz veins in Jiaodong
Pyrite in Wulong
Pyrrhotite in Wulong

Figure 11

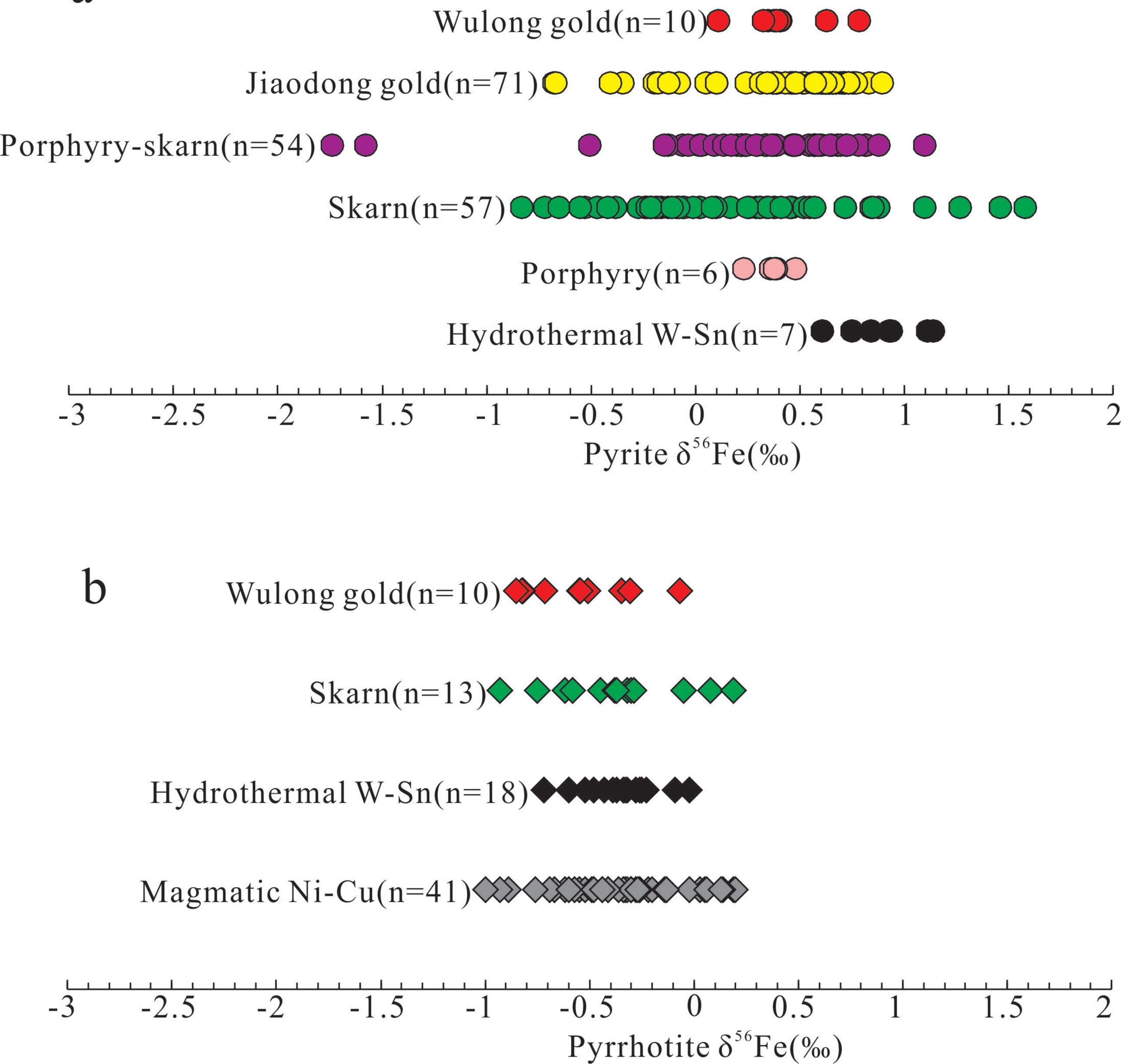
a
Wulong gold(n=10)
Jiaodong gold(n=71)
Porphyry-skarn(n=54)
Skarn(n=57)
Porphyry(n=6)
Hydrothermal W-Sn(n=7)
-3
-2.5
-2
-1.5
-1
-0.5
0
0.5
1
1.5
2
Pyrite δ56Fe(‰)
b
Wulong gold(n=10)
Skarn(n=13)
Hydrothermal W-Sn(n=18)
Magmatic Ni-Cu(n=41)
-3
-2.5
-2
-1.5
-1
-0.5
0
0.5
1
1.5
2
Pyrrhotite δ56Fe(‰)